OAK RIDGE
NATIONAL LABORATORY
MANAGED BY UT-BATTELLE
FOR THE DEPARTMENT OF ENERGY

ORNL/TM-2014/12

Impact of the High Flux Isotope Reactor HEU to LEU Fuel Conversion on Cold Source Nuclear Heat Generation Rates

March 2014

Prepared by

David Chandler
Research Reactors Division
Oak Ridge National Laboratory

Approved for public release;
distribution is unlimited.

UT-BATTELLE
ORNL-27 (4-00)

DOCUMENT AVAILABILITY

Reports produced after January 1, 1996, are generally available free via US Department of Energy (DOE) SciTech Connect.

Website http://www.osti.gov/scitech/

Reports produced before January 1, 1996, may be purchased by members of the public from the following source:

National Technical Information Service
5285 Port Royal Road
Springfield, VA 22161
Telephone 703-605-6000 (1-800-553-6847)
TDD 703-487-4639
Fax 703-605-6900
E-mail info@ntis.gov
Website http://www.ntis.gov/support/ordernowabout.htm

Reports are available to DOE employees, DOE contractors, Energy Technology Data Exchange representatives, and International Nuclear Information System representatives from the following source:

Office of Scientific and Technical Information
PO Box 62
Oak Ridge, TN 37831
Telephone 865-576-8401
Fax 865-576-5728
E-mail reports@osti.gov
Website http://www.osti.gov/contact.html

This report was prepared as an account of work sponsored by an agency of the United States Government. Neither the United States Government nor any agency thereof, nor any of their employees, makes any warranty, express or implied, or assumes any legal liability or responsibility for the accuracy, completeness, or usefulness of any information, apparatus, product, or process disclosed, or represents that its use would not infringe privately owned rights. Reference herein to any specific commercial product, process, or service by trade name, trademark, manufacturer, or otherwise, does not necessarily constitute or imply its endorsement, recommendation, or favoring by the United States Government or any agency thereof. The views and opinions of authors expressed herein do not necessarily state or reflect those of the United States Government or any agency thereof.

ORNL/TM-2014/12

Research Reactors Division

IMPACT OF THE HIGH FLUX ISOTOPE REACTOR HEU TO LEU FUEL CONVERSION ON COLD SOURCE NUCLEAR HEAT GENERATION RATES

David Chandler

Date Published: March 2014

Prepared by
OAK RIDGE NATIONAL LABORATORY
Oak Ridge, Tennessee 37831-6283
managed by
UT-BATTELLE, LLC
for the
US DEPARTMENT OF ENERGY
under contract DE-AC05-00OR22725

CONTENTS

Page

LIST OF FIGURES v
LIST OF TABLES vii
ACKNOWLEDGMENTS ix
ACRONYMS AND ABBREVIATIONS xi
ABSTRACT xiii
1. INTRODUCTION 1
2. GEOMETRY AND COMPUTATIONAL MODELS 3
2.1 CODES AND METHODS 3
2.2 MODEL GEOMETRY 3
3. METHODS 12
3.1 NUCLEAR DATA 12
3.2 NEUTRON FLUX 13
3.3 PROMPT RADIATION HEAT DEPOSITION 13
3.4 DELAYED PHOTON HEAT DEPOSITION 14
3.5 DELAYED BETA HEAT DEPOSITION 15
3.6 SILICON PRODUCTION RATES 15
3.7 MATHEMATICAL FITS 16
4. RESULTS 18
4.1 SUMMARY OF MCNP RUNS 18
4.2 BEGINNING-OF-CYCLE HEAT GENERATION RESULTS 18
4.3 END-OF-CYCLE HEAT GENERATION RESULTS 23
4.4 FITS TO HEAT GENERATION RATES 27
4.5 SILICON PRODUCTION RATE RESULTS 35
4.6 NEUTRON FLUX IN LH_2 HEMISPHERE RESULTS 36
5. SUMMARY AND CONCLUSIONS 41
6. REFERENCES 43
APPENDIX. METHODS AND PREVIOUS CALCULATION COMPARISONS A-1

LIST OF FIGURES

Figure		Page
Fig. 1.	High Flux Isotope Reactor core mock-up and cold source moderator vessel.	1
Fig. 2.	Cross section of MCNP as-modeled geometry.	4
Fig. 3.	Elevation view of horizontal beam tube 4 about 10 (a), 18 (b), 20 (c), and 25 (d) cm from the midpoint between horizontal beam tube 1 and horizontal beam tube 4.	5
Fig. 4.	Beginning-of-cycle heat generation rates in LH_2 hemisphere.	20
Fig. 5.	Beginning-of-cycle heat generation rates in LH_2 sections 2–6.	20
Fig. 6.	Beginning-of-cycle heat generation rates in aluminum sections.	22
Fig. 7.	End-of-cycle heat generation rates in LH_2 hemisphere.	24
Fig. 8.	End-of-cycle heat generation rates in LH_2 sections 2–6.	25
Fig. 9.	End-of-cycle heat generation rates in aluminum sections.	26
Fig. 10.	Beginning-of-cycle LH_2 hemisphere neutron energy deposition (W/g): HEU (a) and LEU (b).	30
Fig. 11.	Beginning-of-cycle LH_2 hemisphere photon energy deposition (W/g): HEU (a) and LEU (b).	30
Fig. 12.	Beginning-of-cycle LH_2 hemisphere total energy deposition (W/g): HEU (a) and LEU (b).	30
Fig. 13.	End-of-cycle LH_2 hemisphere neutron energy deposition (W/g): HEU (a) and LEU (b).	31
Fig. 14.	End-of-cycle LH_2 hemisphere photon energy deposition (W/g): HEU (a) and LEU (b).	31
Fig. 15.	End-of-cycle LH_2 hemisphere total energy deposition (W/g): HEU (a) and LEU (b).	31
Fig. 16.	Beginning-of-cycle aluminum hemisphere 85 HEU to 100 LEU ratio: neutron (a), beta (b), photon (c), and total (d).	33
Fig. 17.	End-of-cycle aluminum hemisphere 85 HEU to 100 LEU ratio: neutron (a), beta (b), photon (c), and total (d).	34
Fig. 18.	Beginning-of-cycle silicon production rates in aluminum sections.	35
Fig. 19.	End-of-cycle silicon production rates in aluminum sections.	36
Fig. 20.	Thermal (E_n < 0.625 eV) neutron flux in LH_2 hemisphere.	37
Fig. 21.	Epithermal (0.1 MeV > E_n > 0.625 eV) neutron flux in LH_2 hemisphere.	37
Fig. 22.	Fast (20 MeV > E_n > 0.1 MeV) neutron flux in LH_2 hemisphere.	38
Fig. 23.	Total neutron flux in LH_2 hemisphere.	38

LIST OF TABLES

Table **Page**

Table 1. Hemispherical region of cold source LH_2 subdivided cell descriptions 7

Table 2. Sections 2–6 of cold source LH_2 subdivided cell descriptions 8

Table 3. Hemispherical region and sections 2–3 of cold source aluminum subdivided cell descriptions..... 9

Table 4. Cold source aluminum regions beyond section 3 cell descriptions..... 10

Table 5. Summary of MCNP calculations..... 18

Table 6. Beginning-of-cycle total heat generation rate summary for the cold source LH_2 regions..... 21

Table 7. Beginning-of-cycle radiation-dependent heat generation rate summary for the cold source LH_2 regions..... 21

Table 8. Beginning-of-cycle total heat generation rate summary for the cold source aluminum regions 22

Table 9. Beginning-of-cycle radiation-dependent heat generation rate summary for the cold source aluminum regions..... 23

Table 10. End-of-cycle total heat generation rate summary for the cold source LH_2 regions 25

Table 11. End-of-cycle radiation-dependent heat generation rate summary for the cold source LH_2 regions 26

Table 12. End-of-cycle total heat generation rate summary for the cold source aluminum regions..... 27

Table 13. End-of-cycle radiation-dependent heat generation rate summary for the cold source aluminum regions 27

Table 14. Fitting coefficients to total heat generation rates in hemispherical part of cold source LH_2 28

Table 15. Fits to total heat generation rates in hemispherical part of cold source LH_2..... 29

Table 16. Fitting coefficients to total heat generation rates in hemispherical part of cold source aluminum..... 32

Table 17. Fit to total heat generation rates in hemispherical part of cold source aluminum..... 32

ACKNOWLEDGMENTS

This work was sponsored by the Global Threat Reduction Initiative, Reduced Enrichment for Research and Test Reactors Program, a program of the National Nuclear Security Administration, US Department of Energy.

The author gratefully acknowledges the technical reviews of this manuscript that were performed by Eva Sunny, Reactor and Nuclear Systems Division, Oak Ridge National Laboratory (ORNL), and David Renfro, Research Reactors Division, ORNL. In addition, the author acknowledges everyone who has contributed to the development of the computational models described in this report including, but certainly not limited to, Germina Ilas, R. T. Primm III, and C. O. Slater (all of or formerly of ORNL). Finally, the author is indebted to Mary Wells, Research Reactors Division, ORNL, for assistance formatting the manuscript.

ACRONYMS AND ABBREVIATIONS

BOC	beginning-of-cycle
CE	control element
CHM	core horizontal midplane
DOE	US Department of Energy
ENDF	Evaluated Nuclear Data File
EOC	end-of-cycle
FP	full reactor power (85 MW for HEU core and 100 MW for LEU core)
FTT	flux trap target region
HB	horizontal beam tube
HEU	high enriched uranium
HFIR	High Flux Isotope Reactor
IFE	inner fuel element
IKE	Institut für Kernenergetik und Energiesysteme (University of Stuttgart, Institute for Nuclear Technology and Energy Systems)
LANL	Los Alamos National Laboratory
LH_2	liquid hydrogen
LEU	low enriched uranium
MCNP	Monte Carlo N-Particle (code)
OFE	outer fuel element
ORIGEN	Oak Ridge Isotope Generation (code)
ORNL	Oak Ridge National Laboratory
SCALE	Standardized Computer Analysis for Licensing Evaluations

ABSTRACT

Under the sponsorship of the US Department of Energy National Nuclear Security Administration, staff members at the Oak Ridge National Laboratory have been conducting studies to determine whether the High Flux Isotope Reactor (HFIR) can be converted from high enriched uranium (HEU) fuel to low enriched uranium (LEU) fuel. As part of these ongoing studies, an assessment of the impact that the HEU to LEU fuel conversion has on the nuclear heat generation rates in regions of the HFIR cold source system and its moderator vessel was performed and is documented in this report. Silicon production rates in the cold source aluminum regions and few-group neutron fluxes in the cold source moderator were also estimated.

Neutronics calculations were performed with the Monte Carlo N-Particle code to determine the nuclear heat generation rates in regions of the HFIR cold source and its vessel for the HEU core operating at a full reactor power (FP) of 85 MW(t) and the reference LEU core operating at an FP of 100 MW(t). Calculations were performed with beginning-of-cycle (BOC) and end-of-cycle (EOC) conditions to bound typical irradiation conditions. Average specific BOC heat generation rates of 12.76 and 12.92 W/g, respectively, were calculated for the hemispherical region of the cold source liquid hydrogen (LH_2) for the HEU and LEU cores, and EOC heat generation rates of 13.25 and 12.86 W/g, respectively, were calculated for the HEU and LEU cores. Thus, the greatest heat generation rates were calculated for the EOC HEU core, and it is concluded that the conversion from HEU to LEU fuel and the resulting increase of FP from 85 MW to 100 MW will not impact the ability of the heat removal equipment to remove the heat deposited in the cold source system.

Silicon production rates in the cold source aluminum regions are estimated to be about 12.0% greater at BOC and 2.7% greater at EOC for the LEU core in comparison to the HEU core. Silicon is aluminum's major transmutation product and affects mechanical properties of aluminum including density, neutron irradiation hardening, swelling, and loss of ductility. Because slightly greater quantities of silicon will be produced in the cold source moderator vessel for the LEU core, these effects will be slightly greater for the LEU core than for the HEU core.

Three-group (thermal, epithermal, and fast) neutron flux results tallied in the cold source LH_2 hemisphere show greater values for the LEU core under both BOC and EOC conditions. The thermal neutron flux in the LH_2 hemisphere for the LEU core is about 12.4% greater at BOC and 2.7% greater at EOC than for the HEU core. Therefore, cold neutron scattering will not be adversely affected and the 4–12 Å neutrons conveyed to the cold neutron guide hall for research applications will be enhanced.

1. INTRODUCTION

The High Flux Isotope Reactor (HFIR) is a multipurpose research reactor located at the Oak Ridge National Laboratory (ORNL) in Oak Ridge, Tennessee, USA. It currently operates at a full reactor power (FP) of 85 MW(t) and provides cold and thermal neutron scattering, isotope production, materials irradiation, and neutron activation analysis capabilities. HFIR was designed to produce a large thermal flux-to-power ratio by including an over-moderated flux trap target region (FTT) in the center of the reactor core and a large beryllium reflector on the outside of the core. On the outside of the FTT are two concentric fuel annuli, an inner fuel element (IFE) and an outer fuel element (OFE). Two concentric poison-bearing control elements (CEs) are situated outside of the fuel elements for safety and regulation purposes, and a large beryllium reflector encompasses the core and CEs. Fig. 1 illustrates the HFIR layout, including photographs of the core and cold source moderator vessel.

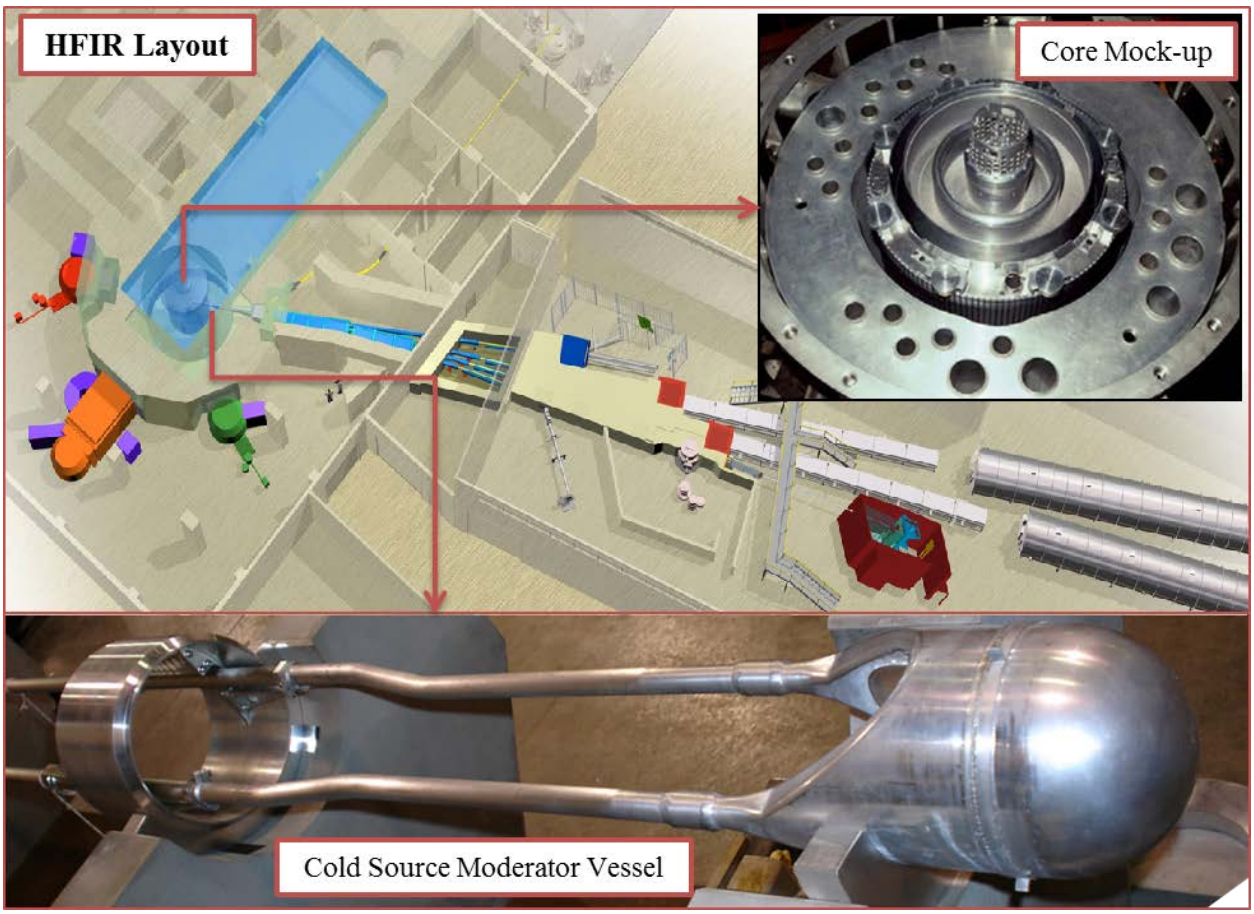

Fig. 1. High Flux Isotope Reactor core mock-up and cold source moderator vessel.

This pressurized, light water–cooled and –moderated flux-trap type reactor uses high enriched uranium (HEU) fuel enriched to about 93 wt % in ^{235}U in the form of U_3O_8 in an aluminum matrix. The IFE is constructed of 171 involute fuel plates, the OFE is constructed of 369 involute fuel plates, and the fuel is nonuniformly distributed along the arc of the involute and encapsulated within Al-6061 cladding. The total loading of a fresh HFIR (HEU) core is about 9.4 kg of ^{235}U, and a typical fuel cycle length ranges from 22 to 26 days depending on the experiment loading.

The beryllium reflector is penetrated by 42 vertical facilities used for irradiation purposes and four horizontal beam tube (HB) experiment facilities that extend outward from the reactor core at the core horizontal midplane (CHM). The beryllium reflector also serves as a neutron moderator by slowing down the high-energy source neutrons. Horizontal beam tube number 4 (HB-4) is an aluminum tube that is aligned on a tangential line about 38.5 cm from the reactor core center line and contains the liquid hydrogen (LH_2) cold source moderator vessel, transfer lines, and vacuum tube. At a temperature of 18–20 Kelvin and a nominal flow rate of 1 L/s, the supercritical hydrogen moderator enters the supply line located on the CHM on the side away from the core and then exits on the side toward the core. Neutron collisions in the supercritical hydrogen further reduce the neutron energies to about 4–12 Å for cold neutron scattering applications. The moderator vessel is shown in Fig. 1.

Under the sponsorship of the US Department of Energy National Nuclear Security Administration, staff members at ORNL have been conducting studies to determine whether HFIR can be converted from HEU fuel to low enriched uranium (LEU) fuel. The proposed LEU fuel will be enriched to 19.75 wt % ^{235}U in the form of U-10Mo, a uranium metal alloyed with molybdenum with the molybdenum composing 10 wt % of the mixture. The fresh core uranium loading will increase from about 10.1 kg (HEU fuel) to about 125 kg (LEU fuel). Due to the self-shielding effects introduced by the large concentration of ^{238}U, the critical mass of ^{235}U will be increased from about 9.4 kg (HEU fuel) to about 25.3 kg (LEU fuel). To maintain the neutron flux at the experiment facilities, FP will need to be increased from 85 MW(t) to 100 MW(t). A more thorough description of the reference LEU design is provided in [1].

Energy (heat) is deposited in the cold source moderator and vessel during reactor operation due to direct neutron and photon (primary, secondary, and delayed fission) sources. Beta heating, due to the decay of ^{28}Al following neutron capture in ^{27}Al, is also considered for the aluminum regions. Neutrons and photons deposit their energy throughout the reactor and, therefore, must be transported in the analyses to determine the spatial energy deposition distribution. However, beta particles have very little penetrating power, so it is assumed that their energy is deposited locally (i.e., at the location where ^{27}Al captures a neutron). Nuclear heat generation calculations are required because this heat, along with any mechanically induced heat, must be removed [2]. A circulator located in the pump module pumps hydrogen through the moderator vessel, and the warm hydrogen returns to the heat exchanger module where it is cooled by helium.

Cold source nuclear heat generation rates were calculated previously for the 85 MW HEU core and reported in [2–4]. The purpose of this report is to compare the nuclear heat generation rates in the cold source for the HEU-loaded HFIR core and the reference LEU-loaded HFIR core operating at 100 MW [1]. Heat deposition due to photons, neutrons, and beta particles (only in aluminum) and the sum of these constituents were calculated in watts per gram for the cold source LH_2 moderator, the cold source moderator vessel, the HB-4 aluminum structure, and other regions of interest including stainless steel screws and titanium wires. However, only the heat generation rates in the cold source LH_2 moderator and the cold source moderator vessel are discussed in this report. Heat generation rates for all regions and corresponding fitting functions are documented in detail in [5].

Silicon production in the aluminum cold source moderator vessel is another concern that is assessed because the build-up of silicon in structural aluminum contributes to mechanical property changes including swelling, hardening, and loss of ductility. As described in more detail in a later section, ^{28}Si is the product of the $^{27}Al(n,\gamma)^{28}Al \rightarrow {}^{28}Si + \beta^-$ reaction. The fast component of the neutron flux displaces atoms and the thermal component generates ^{28}Si, and both of these lead to swelling and embrittlement. Thus, the thermal-to-fast neutron flux ratio is important when performing neutron damage assessments. Because the thermal-to-fast neutron flux ratio is very high in the permanent beryllium reflector and silicon will accrue with irradiation exposure, the impact that the conversion has on the silicon production rates in the aluminum moderator vessel is also assessed in this report.

2. GEOMETRY AND COMPUTATIONAL MODELS

2.1 CODES AND METHODS

The enhanced HEU models [1] based on the cycle 400 HEU model of the HFIR fresh core [6] and the 2011 models for the LEU core [1] were used for this set of comparison studies. Previous HEU to LEU comparison studies documented in [7] and [8] also made use of these models. The Monte Carlo N-Particle 5 (MCNP5) code, version 1.5.1 [9], which is a Monte Carlo-based neutron-photon-electron transport code developed and maintained at the Los Alamos National Laboratory (LANL), was used in this study to perform coupled neutron-photon calculations. The transport calculations made use of the Evaluated Nuclear Data File (ENDF) cross section libraries.

Calculations were performed with beginning-of-cycle (BOC) and end-of-cycle (EOC) conditions to bound typical HFIR operating conditions. The EOC inputs were obtained from previous depletion studies [1] performed with VESTA [10], a Monte Carlo-based depletion tool developed and maintained at Institut de Radioprotection et de Sûreté Nucléaire (French Institute for Radiological Protection and Nuclear Safety), which was validated against HFIR post-irradiation, spatially dependent uranium isotopic measurements [11] and compared to calculations performed with the Standardized Computer Analysis for Licensing Evaluations code package (SCALE) [12] in [13]. The fuel, CEs, and curium targets (applicable only to the LEU inputs) were depleted, and CE withdrawal was simulated during the VESTA calculations.

Each of the HEU and LEU, BOC and EOC, models were further enhanced by subdividing the cold source moderator, moderator vessel, and beam tube into smaller zones to capture the spatially dependent specific nuclear heat deposition rates [4]. MCNP tally cards were used to obtain the desired output and MATLAB [14], a commercial software package, was used to organize, post-process, and plot the results provided by the MCNP runs.

2.2 MODEL GEOMETRY

The BOC calculations are based on fresh fuel, and the CEs are at their initial symmetrical critical positions of 18.0 and 19.5 in. withdrawn, respectively, for the HEU and LEU calculations. The CEs are fully withdrawn (~27 in. withdrawn) and the EOC fuel compositions are used for the EOC calculations. During the cycle, the CEs are moved vertically to maintain the reactor's critical state. The inner element moves downward and the outer plates (four) move upward, increasing the distance between the absorbing regions of the elements and the CHM, thus opening a neutron "window" (aluminum only section of CEs) and allowing more source neutrons to leak into the reflector and reflect back into the core. The symmetrical positions of 18.0 and 19.5 in. withdrawn correspond, respectively, to 1.0 and 2.5 in. gaps between the CHM and the gray (tantalum-aluminum) regions. Thus, the neutron windows are 2.0 in. (i.e., 2 × 1.0 in.) in length for the HEU BOC calculation and 5.0 in. in length for LEU BOC calculation.

For both the HEU and LEU inputs, the fuel elements are modeled by volumetrically homogenizing the fuel meat, filler, clad, and water in between the fuel plates. The IFE is divided into 8 radial regions and 19 axial regions, and the OFE is divided into 9 radial regions and 19 axial regions. The fuel elements are divided radially to represent the different effective fuel concentrations in the radial direction, and they are divided axially to model the EOC spatially dependent (depleted) fuel compositions. An x-y cross section of the MCNP model at the CHM is provided in Fig. 2.

The cold source vessel and moderator geometry, as provided in the reference MCNP models, was further subdivided into finer regions to determine the spatially dependent nuclear heat generation rates. The

subdivided cold source model described in [4] was used for these changes, and the next three paragraphs are paraphrased from [4].

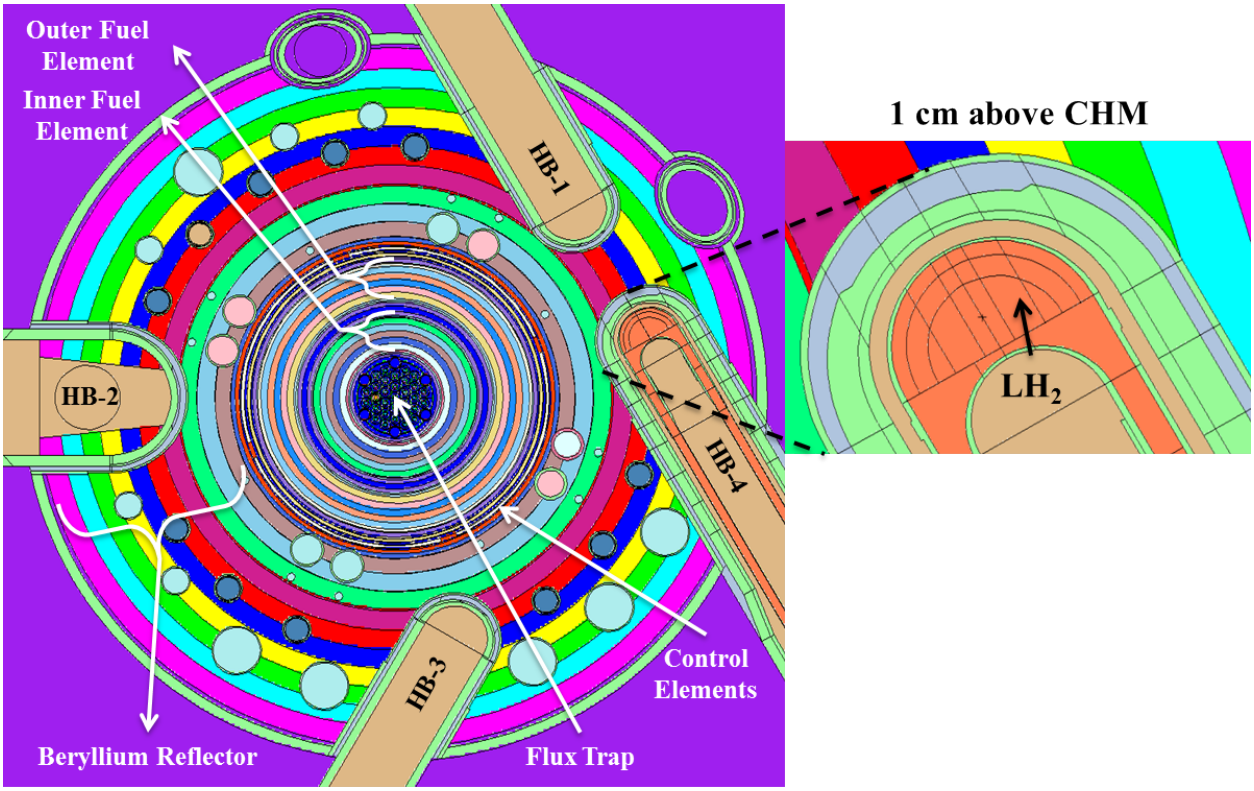

Fig. 2. Cross section of MCNP as-modeled geometry.

The hemispherical portion of the cold source moderator and the adjoining 0.12446 cm thick cylindrical disk were previously described by two cells (numbered 86011 and 86012 in the MCNP model). These cells were replaced by 36 cells numbered 95001 through 95036. The hemisphere was subdivided into three equal-volume regions, and these radii also subdivided the adjoining 0.12446 cm thick cylindrical disk. Each of the three subvolumes was subdivided into 12 azimuthal segments of equal volume within a given subvolume (because the cylinder was not subdivided into three equal subvolumes, the volumes of the cells comprising the union of the hemisphere and cylinder differed from one subvolume to the next).

The cells composing the hemispherical portion of the vessel (numbered 86021 and 86022) were partitioned into 12 azimuthal segments (numbered 86021–86032). The vessel cells numbered 86041 and 86042 were further subdivided into eight cells (numbered 86041–86048) having unequal volumes. Likewise, the cells numbered 86061 and 86062 were further subdivided into eight cells (numbered 86061–86068). Moderator cells numbered 86051 and 86052 were further subdivided into eight cells (numbered 86051–86058) having unequal volumes. Cells 86101, 86102, 86111, and 86112 were renamed 86111 through 86114.

The cells numbered 86091 and 86092 were further subdivided into 16 subcells (numbered 86091–86106). The region extends from a point 15.09268 cm from the start of the beam tube to a point 22.86 cm from the start of the beam tube. The first eight subcells cover the region from 15.09268 cm to 19.05 cm, and the last eight cover the region from 19.05 cm to 22.86 cm. Of the last eight, only four have nonzero volumes because, as seen in Fig. 3c, upper and lower segments are not present at this location. As seen in Fig. 2, the azimuthal angle is measured from a vector parallel to the radius vector from the core center to

the origin of HB-4. Thus, the first azimuth is away from the core and above the tube midplane, and the last azimuth is away from the core and below the tube midplane. Volumes of the subdivided regions were stochastically computed, and averaged values were used when the volumes could not be easily computed analytically.

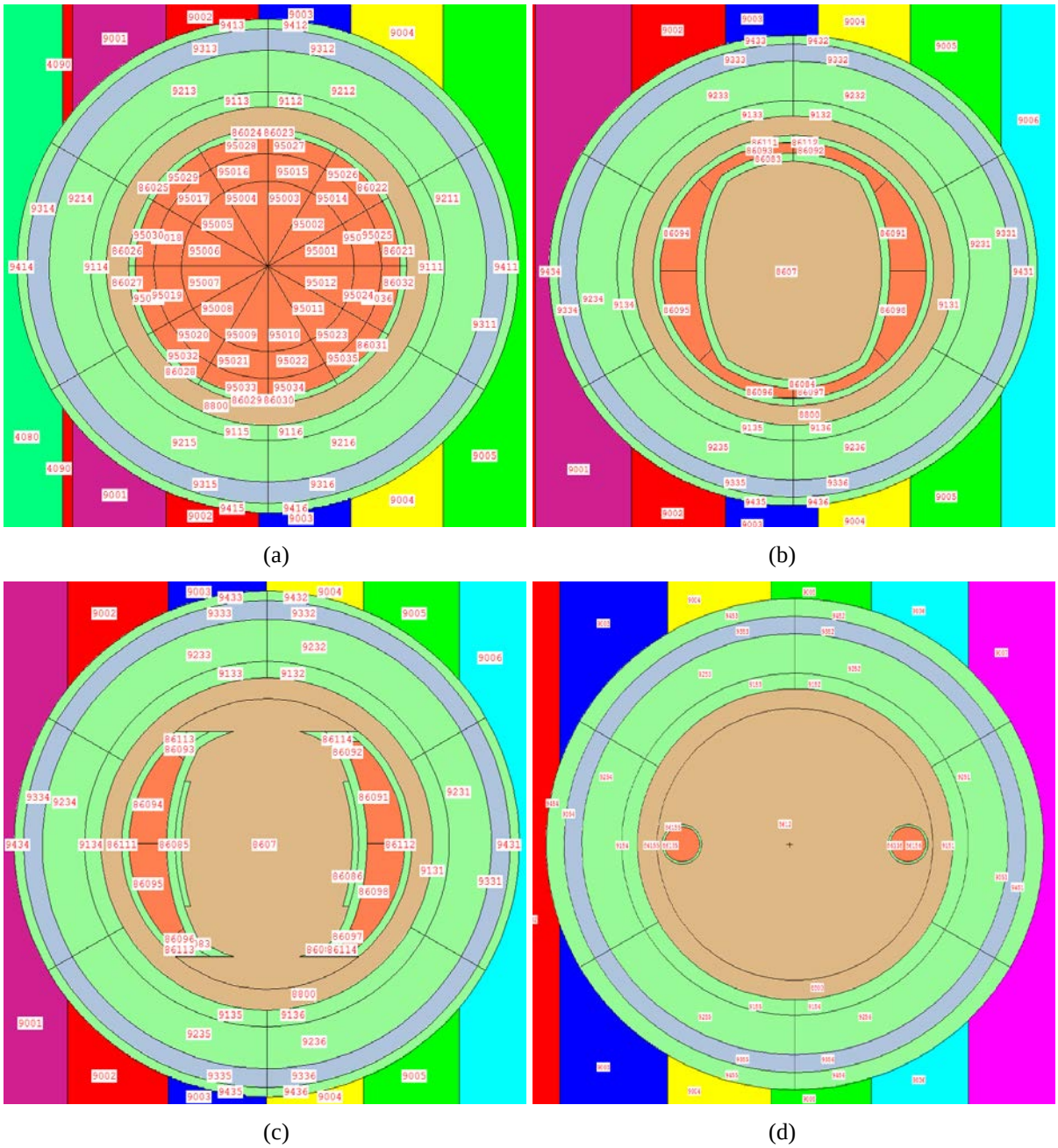

(a) (b)

(c) (d)

Fig. 3. Elevation view of horizontal beam tube 4 about 10 (a), 18 (b), 20 (c), and 25 (d) cm from the midpoint between horizontal beam tube 1 and horizontal beam tube 4.

The beam tube origin is defined as being the intersection of the plane midway between HB-1 and HB-4 and on the centerline for HB-4. The r = 0 point lies on the centerline of HB-4 and is located 11.43 cm from the beam tube origin. The maximum value of r for the LH_2 moderator is 4.6736 cm. The azimuthal angle, θ, is measured from a vector parallel to the radius vector from the core center to the beam tube

origin. Thus, for a given distance along the beam tube, the zero-degree value will be a coordinate of the point farthest from the core, and the 180-degree value will be a coordinate of the point closest to the core. Refer to Fig. 3 for two-dimensional slices through HB-4 illustrating the subdivided cold source moderator and vessel regions. Data including the volumes of the cells are provided for the various regions in Table 1–Table 4. Note that the identifiers in these tables are used to identify the cells in the plots in Section 4.

Table 1. Hemispherical region of cold source LH_2 subdivided cell descriptions

Identifier	Cell	Volume (cm^3)	Mass (g)	Radius (cm)	Angle (deg.)
1	95001	6.28112	0.45601	2.57198	15
2	95002	6.28112	0.45601	2.57198	45
3	95003	6.28112	0.45601	2.57198	75
4	95004	6.28112	0.45601	2.57198	105
5	95005	6.28112	0.45601	2.57198	135
6	95006	6.28112	0.45601	2.57198	165
7	95007	6.28112	0.45601	2.57198	195
8	95008	6.28112	0.45601	2.57198	225
9	95009	6.28112	0.45601	2.57198	255
10	95010	6.28112	0.45601	2.57198	285
11	95011	6.28112	0.45601	2.57198	315
12	95012	6.28112	0.45601	2.57198	345
13	95013	6.13995	0.44576	3.70944	15
14	95014	6.13995	0.44576	3.70944	45
15	95015	6.13995	0.44576	3.70944	75
16	95016	6.13995	0.44576	3.70944	105
17	95017	6.13995	0.44576	3.70944	135
18	95018	6.13995	0.44576	3.70944	165
19	95019	6.13995	0.44576	3.70944	195
20	95020	6.13995	0.44576	3.70944	225
21	95021	6.13995	0.44576	3.70944	255
22	95022	6.13995	0.44576	3.70944	285
23	95023	6.13995	0.44576	3.70944	315
24	95024	6.13995	0.44576	3.70944	345
25	95025	6.10754	0.44341	4.39803	15
26	95026	6.10754	0.44341	4.39803	45
27	95027	6.10754	0.44341	4.39803	75
28	95028	6.10754	0.44341	4.39803	105
29	95029	6.10754	0.44341	4.39803	135
30	95030	6.10754	0.44341	4.39803	165
31	95031	6.10754	0.44341	4.39803	195
32	95032	6.10754	0.44341	4.39803	225
33	95033	6.10754	0.44341	4.39803	255
34	95034	6.10754	0.44341	4.39803	285
35	95035	6.10754	0.44341	4.39803	315
36	95036	6.10754	0.44341	4.39803	345

Table 2. Sections 2–6 of cold source LH_2 subdivided cell descriptions

Identifier	Cell	Volume (cm^3)	Mass (g)	Angle (deg.)
		Section 2		
1	86051	19.51130	1.41652	22.5
2	86052	14.12620	1.02556	67.5
3	86053	14.12620	1.02556	112.5
4	86054	19.51130	1.41652	157.5
5	86055	19.51130	1.41652	202.5
6	86056	14.12620	1.02556	247.5
7	86057	14.12620	1.02556	292.5
8	86058	19.51130	1.41652	337.5
		Section 3		
9	86091	13.64330	0.99050	22.5
10	86092	2.91403	0.21156	67.5
11	86093	2.91403	0.21156	112.5
12	86094	13.64330	0.99050	157.5
13	86095	13.64330	0.99050	202.5
14	86096	2.91403	0.21156	247.5
15	86097	2.91403	0.21156	292.5
16	86098	13.64330	0.99050	337.5
		Section 4		
17	86099	7.96407	0.57819	-
18	86106	7.96407	0.57819	-
19	86102	7.96407	0.57819	-
20	86103	7.96407	0.57819	-
		Section 5		
21	86135	4.82639	0.35040	-
22	86136	4.82639	0.35040	-
		Section 6		
23	86137	217.18700	15.76778	-
24	86138	217.18700	15.76778	-

Table 3. Hemispherical region and sections 2–3 of cold source aluminum subdivided cell descriptions

Identifier	Cell	Volume (cm^3)	Mass (g)	Angle (deg.)
		Hemisphere		
1	86021	2.27333	6.13799	15.0
2	86022	2.27333	6.13799	45.0
3	86023	2.27333	6.13799	75.0
4	86024	2.27333	6.13799	105.0
5	86025	2.27333	6.13799	135.0
6	86026	2.27333	6.13799	165.0
7	86027	2.27333	6.13799	195.0
8	86028	2.27333	6.13799	225.0
9	86029	2.27333	6.13799	255.0
10	86030	2.27333	6.13799	285.0
11	86031	2.27333	6.13799	315.0
12	86032	2.27333	6.13799	345.0
		Section 2		
13	86041	1.99551	5.38788	22.5
14	86042	2.58831	6.98844	67.5
15	86043	2.58831	6.98844	112.5
16	86044	1.99551	5.38788	157.5
17	86045	1.99551	5.38788	202.5
18	86046	2.58831	6.98844	247.5
19	86047	2.58831	6.98844	292.5
20	86048	1.99551	5.38788	337.5
		Section 3		
21	86061	3.66475	9.89483	22.5
22	86062	3.66475	9.89483	67.5
23	86063	3.66475	9.89483	112.5
24	86064	3.66475	9.89483	157.5
25	86065	3.66475	9.89483	202.5
26	86066	3.66475	9.89483	247.5
27	86067	3.66475	9.89483	292.5
28	86068	3.66475	9.89483	337.5

Table 4. Cold source aluminum regions beyond section 3 cell descriptions

Identifier	Cell	Volume (cm^3)	Mass (g)
29	86083	17.30090	46.71243
30	86084	17.30090	46.71243
31	86085	3.13850	8.47395
32	86086	3.13850	8.47395
33	86111	15.17320	40.96764
34	86112	15.17320	40.96764
35	86113	4.69875	12.68663
36	86114	4.69875	12.68663
37	86145	2.53774	6.85190
38	86146	2.53774	6.85190
39	86155	0.43096	1.16359
40	86156	0.43096	1.16359
41	86157	58.17930	157.08411
42	86158	58.17930	157.08411

3. METHODS

3.1 NUCLEAR DATA

The MCNP calculations made use of the ENDF/B-VII.0 cross sections. A modified version of the ENDF/B-VII.0 cross section library for ^{27}Al, which is documented in [15], was created for these studies to include the 1.779 MeV photon associated with the decay of ^{28}Al atoms that are created by neutron absorption in ^{27}Al. Previous calculations [2–4] made use of a modified ^{27}Al cross section library based on ENDF/B-V data. The newly constructed library (based on ENDF/B-VII.0) was created and tested in a manner similar to that used for the previous library (based on ENDF/B-V) [16].

When the stable ^{27}Al isotope captures a neutron, an ^{28}Al nucleus is produced. Aluminum-28 has a half-life of about 2.24 minutes [17] and undergoes beta decay, creating an excited ^{28}Si nucleus that emits a photon as it decays to a stable state:

$$ {}^{1}_{0}n + {}^{27}_{13}Al \rightarrow {}^{28}_{13}Al \rightarrow {}^{28}_{14}Si + \beta^{-} + \gamma \ . $$

Because every ^{27}Al(n,γ)^{28}Al reaction produces a photon, the original ^{27}Al photon production cross sections were modified by adding the ^{27}Al(n,γ)^{28}Al cross section to the original photon production cross section:

$$ \sigma_{pp}^{modified} = \sigma_{pp}^{original} + \sigma_{(n,\gamma)} \ . $$

An additional photon production reaction was added to the ENDF/B-VII.0 library and was defined such that a 1.7791 MeV photon would be emitted from the location of neutron capture in ^{27}Al. Thus, the delayed photons are treated as regular secondary photons and are transported in the MCNP runs to determine where in the system their energy will be deposited. Using this cross section library eliminates the need to perform activation calculations in a code like the SCALE Oak Ridge Isotope Generation code (ORIGEN) [12] to generate a photon source distribution for use in a follow-on MCNP fixed source photon run.

According to the National Nuclear Data Center [17], the energy of the emitted photon is 1.77885 ± 0.00003 MeV, and a value of 1.7791 MeV was used here. This difference of 0.014% in energy has negligible impact on the results. Verification calculations and more details on the construction of this library are provided in [15].

Under standard temperature and pressure conditions, hydrogen gas is 75% orthohydrogen and 25% parahydrogen. However at lower temperatures, the equilibrium state is composed of more parahydrogen. The cold source LH_2 is specified as a mixture of 65% orthohydrogen and 35% parahydrogen with a density of 0.0726 g/cm^3, which is consistent with previous cold source heat generation rate calculations [2–4]. In these previous calculations, unreleased (at the time) cross sections for the LH_2 based on the LANL evaluation of the Institut für Kernenergetik und Energiesysteme (IKE) data from Germany were used. The calculations performed and documented here used the ENDF/B-VII.0 cross sections. Parametric studies were performed to compare the average nuclear heat generation rates in the LH_2 for a calculation using the IKE cross sections to one using the ENDF/B-VII.0 cross sections. Differences of 0.37% and 0.14%, respectively, were calculated for neutron and photon heating. This and other method development calculations are described in more detail in the Appendix.

3.2 NEUTRON FLUX

For each of the MCNP runs, the neutron fluxes were tabulated in a three-energy group structure with the upper energy boundaries being 6.25×10^{-07}, 0.100, and 20.0 MeV and calculated with track length estimate of neutron cell flux tallies (F4:N). The units of a cell flux tally result are particles per cm^2 per starting particle, and the physical quantity calculated by MCNP is given by [9]

$$\bar{\phi}_V = \frac{1}{V}\int dE \int dt \int dV \int d\Omega\, \psi(\vec{r}, \hat{\Omega}, E, t) \ ,$$

where

$\bar{\phi}_V$	=	volume averaged flux in the cell (particles/cm^2),
V	=	volume of the cell (cm^3),
$\psi(\vec{r}, \hat{\Omega}, E, t)$	=	angular flux (particles/cm^2/sh/MeV/steradian),
$\vec{r}$	=	position vector (cm),
$\hat{\Omega}$	=	direction vector,
E	=	energy (MeV),
t	=	time (sh; 1 sh = 10^{-8} s).

MCNP tallies are normalized per starting particle (i.e., per source fission neutron), and therefore, the tally results must be multiplied by the fission neutron source strength. The fission neutron source strength is defined by

$$Sn\left(\frac{fission\ neutrons}{second}\right) = \frac{P(W) \times \bar{\upsilon}(n/fission)}{e(J/MeV) \times Q(MeV/fission) \times k_{eff}} \ .$$

In the source strength equation, P is the reactor power in watts, $\bar{\upsilon}$ is the average number of neutrons produced per fission reaction, e is a unit conversion factor (1.602177×10^{-13} J/MeV), and Q is the average recoverable energy. A value of 200.7 MeV/fission was used here as the average recoverable energy. Values of 2.440 and 2.456, respectively, were used for the average number of neutrons produced per fission for the HEU and LEU cores. Thus, source strengths of 6.44987×10^{18} and 7.63784×10^{18} s^{-1}, respectively, were used for the 85 MW HEU and 100 MW LEU cases.

3.3 PROMPT RADIATION HEAT DEPOSITION

Track length estimate of energy deposition tallies (type 6) are used to calculate the neutron, (F6:N), photon (F6:P), or combined neutron plus photon (F6:N,P) energy deposition. For these studies, the neutron and photon tallying were performed separately to assess the importance of each with respect to the total energy deposition.

The units corresponding to the F6 tally are megaelectron volts per gram and the desired units are watts per gram, so the tally multiplier required for these tallies is the product of the source strength (s^{-1}) and the unit conversion factor 1.602177×10^{-13} W-s/MeV. The physical quantity calculated by MCNP for the track length estimate of energy deposition tally is given as [9]

$$H_t = \frac{\rho_a}{m}\int dE \int dt \int dV \int d\Omega\, \sigma_t(E) H(E) \psi(\vec{r}, \hat{\Omega}, E, t) \ ,$$

where

H_t = total energy deposition in cell (MeV/g),
ρ_a = atom density (atoms/barn-cm),
m = cell mass (g),
σ_t = microscopic total cross section (barns),
H = heating number (MeV/collision).

Energy deposition as calculated with the F6:N tally accounts for the kinetic energy of neutrons and fission products deposited in the cell being tallied on. Fission products are not transported and thus deposit their energy in the fuel regions. Neutrons are transported and deposit their kinetic energy throughout the system. Energy deposition due to prompt photons released following a fission event and capture photons emitted following a neutron capture event (if photon production data are available for the isotope) are tallied when using the F6:P tally. As previously described, the 1.779 MeV ^{28}Si photon is treated as a regular secondary photon and is thus also accounted for in the F6:P tally.

3.4 DELAYED PHOTON HEAT DEPOSITION

Delayed fission product photons from the decay of fission products are not included in MCNP photon production cross sections, so the delayed photon source is typically determined from a separate calculation with a code like ORIGEN. Then a second MCNP calculation is run in photon transport only mode with the delayed source specified. Previous cold source calculations [2–4] used a specialized ^{235}U cross section library based on ENDF/B-V data which was modified to include the energy dependent delayed fission product photons as regular secondary photons. Although this cross section library is very useful, it underestimates the heat generation rates due to decay photons, and it is based on the older ENDF/B-V data. Also, it only accounts for delayed ^{235}U fissions, which is sufficient for the HEU calculations but not for the LEU calculations.

The approach used to calculate the delayed photon heat generation rates in the calculations documented in this report was first adopted in [15] and [18] for HFIR analysis and is based on [19] and [20]. The photon heating tallies previously described (F6:P) were used to calculate the photon heat generation rates due to the prompt photons. The ENDF Q-values for delayed photons and prompt photons are 6.33 and 6.97 MeV/fission, respectively. Assuming the delayed photon energy spectrum is the same as that of the prompt photon energy spectrum, then the spatially dependent energy deposition will be the same. Therefore, the delayed photon energy deposition can be calculated by multiplying the prompt photon energy deposition by the ratio of the delayed Q-value to the prompt Q-value:

$$H_{d\gamma} = H_{p\gamma}\left(\frac{Q_{d\gamma}}{Q_{p\gamma}}\right) = H_{p\gamma}\left(\frac{6.33}{6.97}\right) .$$

The pikmt photon-production bias card is used to observe the heat deposition due to fission reactions only with biasing the neutron-induced photons. The following pikmt card was used for the HEU calculations.

```
pikmt 92235.70 1 18001 1
```

For this particular example, the photon from ZAID 92235.70 (^{235}U ENDF/B-VII.0 cross section library) will be produced from fission only (the MT reaction identifier 18001). No photons are produced from any other isotopes in the problem. It is valid to only use the ^{235}U isotope for the HEU core pikmt inputs because ^{235}U dominates the fission process in the HEU core, the ^{238}U content is very small, and the plutonium build-in is very low (see Table 18 in [1]).

Due to the increased loading of ^{238}U in the LEU core and the increased build-in of the plutonium isotopes, additional isotopes were added to the pikmt card used for the LEU calculations. The following pikmt card was used for the LEU calculations.

```
pikmt 92234.70 1 18001 1
      92235.70 1 18001 1
      92236.70 1 18001 1
      92238.70 1 18001 1
      92237.70 1 18001 1
      93237.70 1 18001 1
      94239.70 1 18001 1
      94240.70 1 18001 1
      94241.70 1 18001 1
```

The pikmt method requires two MCNP runs to calculate the heat deposition in the cold source regions: a standard run to calculate the heat deposition due to neutrons, beta particles, prompt photons, and capture photons and a pikmt run to calculate the heat deposition due to delayed photons (with inference of the prompt photon heat deposition).

3.5 DELAYED BETA HEAT DEPOSITION

As previously described, neutron capture in ^{27}Al results in the formation of an ^{28}Al nucleus (2.24 min half-life), which undergoes beta decay, creating an excited ^{28}Si nucleus that gives off a photon as it relaxes to the ground state. The average beta energy is 1.247 MeV, and because beta radiation has very little penetrating power and can be stopped by a few millimeters of aluminum, it is assumed that all of its energy is deposited at the site of interaction (i.e., locally deposited). Beta heating rates in the aluminum regions were calculated with track length estimate of neutron cell flux tallies (F4:N) that were described previously.

For the 85 MW HEU and 100 MW LEU cases, tally multipliers of 2.87610×10^4 and 3.40584×10^4 (W-cm^2)/(barn-gram), respectively, were used with the ^{27}Al(n,γ) ^{28}Al ENDF/B-VII.0 capture cross sections (MT 102). The tally multipliers were calculated as follows:

$$\begin{aligned}\beta\ heating\ in\ Al\ tally\ multiplier \\ &= Sn\left(\frac{1}{s}\right)\left(\frac{1.602177\times10^{-13}W-s}{MeV}\right)\left(\frac{0.602214\ cm^2}{barn-mole}\right)\left(\frac{mole}{26.982\ g}\right)\left(\frac{1.247MeV}{\beta\ decay}\right) \\ &= 4.45917\times10^{-15}(Sn)\left(\frac{W-cm^2}{barn-g}\right)\ .\end{aligned}$$

Therefore, the beta heating in aluminum was estimated as follows:

$$H_\beta = 4.45917\times10^{-15}(Sn)\left[\int \sigma_{n,\gamma}(E)\phi(E)dE\right]\left({}^{W}/_{g}\right)\ .$$

3.6 SILICON PRODUCTION RATES

Silicon production rates [1/(g-s)] were calculated in the aluminum regions using type 4 tallies and the ^{27}Al(n,γ) ^{28}Al ENDF/B-VII.0 cross sections (MT 102). The silicon production rates were calculated similarly to the beta energy deposition rates, but a different multiplier was used. The tally multipliers used to calculate the silicon production rates were calculated as follows:

$$Si\ production\ in\ Al\ tally\ multiplier = Sn\left(\frac{1}{s}\right)\left(\frac{0.602214\ cm^2}{barn - mole}\right)\left(\frac{mole}{26.982\ g}\right)$$
$$= 2.23191 \times 10^{-02}(Sn)\left(\frac{cm^2}{barn - g}\right) .$$

Therefore, the silicon production rate was estimated as follows:

$$Si = 2.23191 \times 10^{-02}(Sn)\left[\int \sigma_{n,\gamma}(E)\phi(E)dE\right]\left(\frac{1}{g - s}\right) .$$

3.7 MATHEMATICAL FITS

The spatially dependent specific heat generation rates were fit with the various mathematical functions as described in [4] for use in follow-on heat transfer and thermal hydraulics calculations. A mathematical function was generated for the first three LH_2 zones. The first zone is the hemispherical shell plus the cylindrical shell between 11.43 and 11.55446 cm from the beam tube origin. The second zone is the annular region between 11.55446 and 15.09268 cm from the beam tube origin, and the third zone is the annular region between 15.09268 and 19.05 cm from the beam tube origin. Similarly, functions were generated for the first three cold source aluminum zones.

For the LH_2 hemispherical region, the heat generation rate is defined as a function of both radial and angular position. The spatially dependent heat generation rates for the other LH_2 zones and all of the cold source aluminum zones are defined as a function of angle only. Linear least square methods were used with the MATLAB programming language to solve for the coefficients in the equations describing the various regions as listed below.

LH_2 Hemisphere

$$H_x\ (W/g) = C_{1,x} + C_{2,x}\ r\cos(\theta) + C_{3,x}\ r\sin(\theta) + C_{4,x}\ r\sin(\theta)\cos(\theta) + C_{5,x}\ r^2\cos(2\theta) + C_{6,x}\ r^2\sin(2\theta) + C_{7,x}\ r^2\sin(2\theta)\cos(2\theta) + C_{8,x}\ r + C_{9,x}\ r^2 + C_{10,x}\ r\cos(2\theta) + C_{11,x}\ r^3\cos(\theta)\cos(2\theta) + C_{12,x}\ r^3\cos(\theta)\sin(2\theta) + C_{13,x}\ r^3\sin(\theta)\cos(2\theta) + C_{14,x}\ r^3\sin(\theta)\sin(2\theta)$$

Other Fitted Regions

$$H_x\ (W/g) = C_{1,x} + C_{2,x}\cos(\theta) + C_{3,x}\sin(\theta) + C_{4,x}\cos(2\theta) + C_{5,x}\sin(2\theta)$$

where

x denotes the heating type (neutron, beta, photon, or total),
C_1–C_i are the fitting coefficients,
r is the radius (r = 0 is 11.43 cm from the HB-4 origin),
θ is the angle measured from a vector parallel to the radius vector from the core center to the beam tube origin.

4. RESULTS

4.1 SUMMARY OF MCNP RUNS

A total of eight MCNP calculations were run to determine the specific nuclear heat generation rates for BOC and EOC 85 MW HEU and 100 MW LEU cores. Two MCNP runs were required for each combination (4 combinations): a standard run to determine the energy deposition due to neutrons, betas, prompt photons, and capture photons and a pikmt run to determine the delayed photon energy deposition.

For all calculations except the two EOC pikmt cases, 1.0 billion active histories were run (5,050 cycles, 200,000 source particles per cycle, and 50 cycles to be skipped before tally accumulation). The two EOC pikmt cases used 750 million active histories (3,800 cycles, 200,000 source particles per cycle, and 50 cycles to be skipped before tally accumulation). Fewer histories were used for the EOC pikmt cases because EOC calculations take longer than BOC calculations and pikmt calculations take longer than standard calculations. Therefore, the EOC pikmt calculations require the most computational time. Also, it was determined that 750 million histories yielded satisfactory statistics for the delayed photon energy deposition calculations. A summary of the eight calculations is provided in Table 5.

Table 5. Summary of MCNP calculations

FP (MW)	Core	Condition	Case	CPUs	Clock time (d)	Active histories	k_{eff}	σ_{keff}
85	HEU	BOC	standard	24	1.63	1.00E+09	0.99716	0.00003
85	HEU	BOC	pikmt	28	2.08	1.00E+09	0.99720	0.00003
85	HEU	EOC	standard	32	2.53	1.00E+09	1.00132	0.00003
85	HEU	EOC	pikmt	24	3.85	7.50E+08	1.00129	0.00003
100	LEU	BOC	standard	24	1.70	1.00E+09	0.99978	0.00003
100	LEU	BOC	pikmt	32	1.76	1.00E+09	0.99980	0.00003
100	LEU	EOC	standard	32	2.65	1.00E+09	0.99819	0.00003
100	LEU	EOC	pikmt	32	2.63	7.50E+08	0.99817	0.00003

4.2 BEGINNING-OF-CYCLE HEAT GENERATION RESULTS

As previously mentioned, the specific nuclear heat generation rates have been calculated for BOC and EOC conditions to bound typical cycle conditions. The specific heat generation rates in the cold source LH_2 and aluminum regions have been calculated for the HEU core operating at an FP of 85 MW and for the reference LEU core operating at an FP of 100 MW in units of watts per gram. For all of the regions of interest, line plots are provided for each of the heat deposition constituents (i.e., neutron heating, photon heating, and beta heating) and for the total heating rates:

$$H_{total}\ (W/g) = H_\beta + H_n + H_\gamma \ ,$$

where

H_β is the heat deposition due to beta radiation (only for the aluminum regions),
H_n is the heat deposition due to neutrons,
H_γ is the heat deposition due to photons (prompt + capture + delayed),
$H_\gamma = H_{\gamma(p+c)} + H_{\gamma d}$.

The BOC total heat generation rates and the heat generation rates by the various radiation types in the cold source LH_2 hemispherical region are shown in Fig. 4. (Refer to Table 1 for brief descriptions of the 36 cells composing the cold source LH_2 hemispherical region.) As shown in Fig. 4, the total heat generation rate in these cells varies from about 9 to about 19 W/g for the two cores. Heat generation rates in sections 2–6 of the cold source LH_2 are illustrated in Fig. 5.

Both Fig. 4 and Fig. 5 show that neutron energy deposition is greater than photon energy deposition in the cold source LH_2 regions for both fuel types. For the BOC configuration, the neutron energy deposition rates are greater for the LEU core and the photon energy deposition rates are greater for the HEU core. The total heat generation rates for the LH_2 regions due to each fuel type are comparable, but on average, they are slightly greater for the LEU core.

It is also important to note the critical CE positions differ for the HEU core and the LEU core. The start-up critical CE position for the LEU core is 19.5 in. in comparison to 18.0 in. for the HEU core. This difference in position increases the distance between the CHM and the absorbing regions of the CEs, thus increasing the probability of neutrons leaking from the core into the reflector and cold source regions.

As shown in Table 6, the average BOC heat generation rates in the hemispherical region of the cold source LH_2 for the HEU and LEU cores are 12.76 and 12.92 W/g, respectively. A comparison of the LH_2 radiation-dependent heat generation rates for the HEU core and the LEU core is provided in Table 7. On average, the BOC heat generation rates in the cold source LH_2 regions for the 100 MW LEU core are about 1% greater than those for the 85 MW HEU core.

The BOC total heat generation rates and the heat generation rates by the various radiation types in the cold source aluminum regions are shown in Fig. 6. (Refer to Table 3 and Table 4 for brief descriptions of cells composing the cold source aluminum regions addressed in this figure.) As shown in Fig. 6, the maximum total heat generation rates in these cells are about 3.9 W/g and 3.4 W/g, respectively, for the HEU and LEU cores.

As shown in Fig. 6, neutron energy deposition is essentially a negligible contributor to the total heat generation rates in aluminum, and most of the energy deposition is due to photon radiation. Beta radiation is a small contributor to the total energy deposition. The beta energy deposition rates are greater for the LEU core, the photon energy deposition rates are greater for the HEU core, and the total heat generation rates for the cold source aluminum regions are greater for the HEU core.

As shown in Table 8, the average BOC heat generation rates in the hemispherical region of the cold source aluminum for the 85 MW HEU and the 100 MW LEU cores are 3.12 and 2.79 W/g, respectively. A comparison of the radiation-dependent nuclear heat generation rates in the aluminum regions for the HEU and LEU cores is provided in Table 9. Photon energy deposition contributes about 85% of the total aluminum heating for the HEU core and 80% for the LEU core, and beta heating contributes to the majority of the remaining percentage in each case.

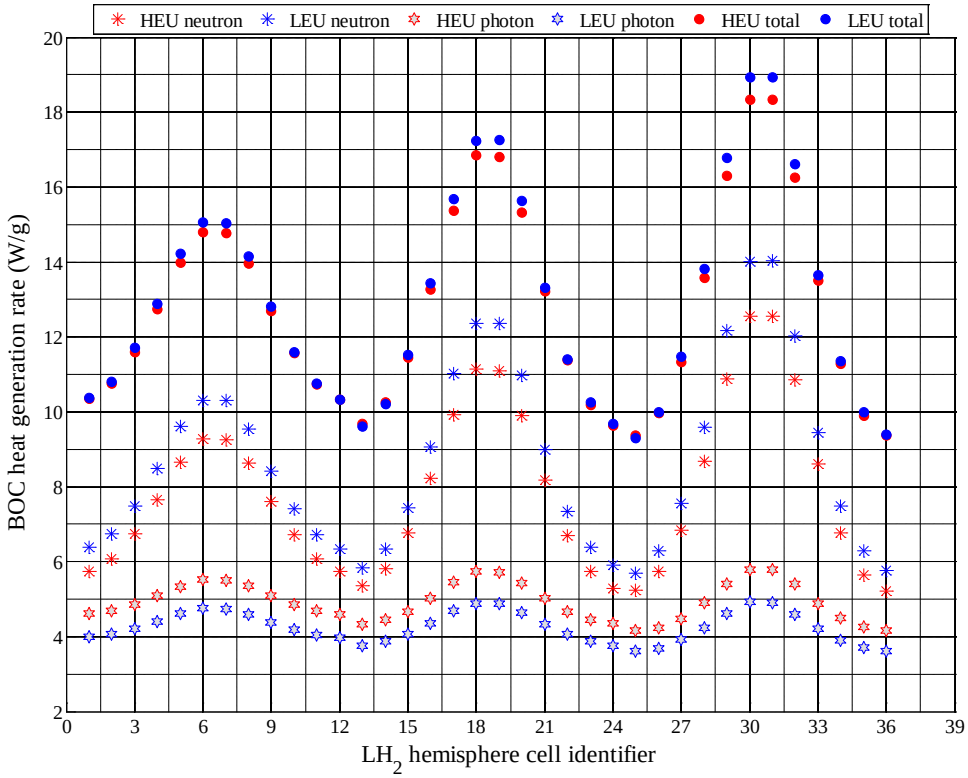

Fig. 4. Beginning-of-cycle heat generation rates in LH_2 hemisphere.

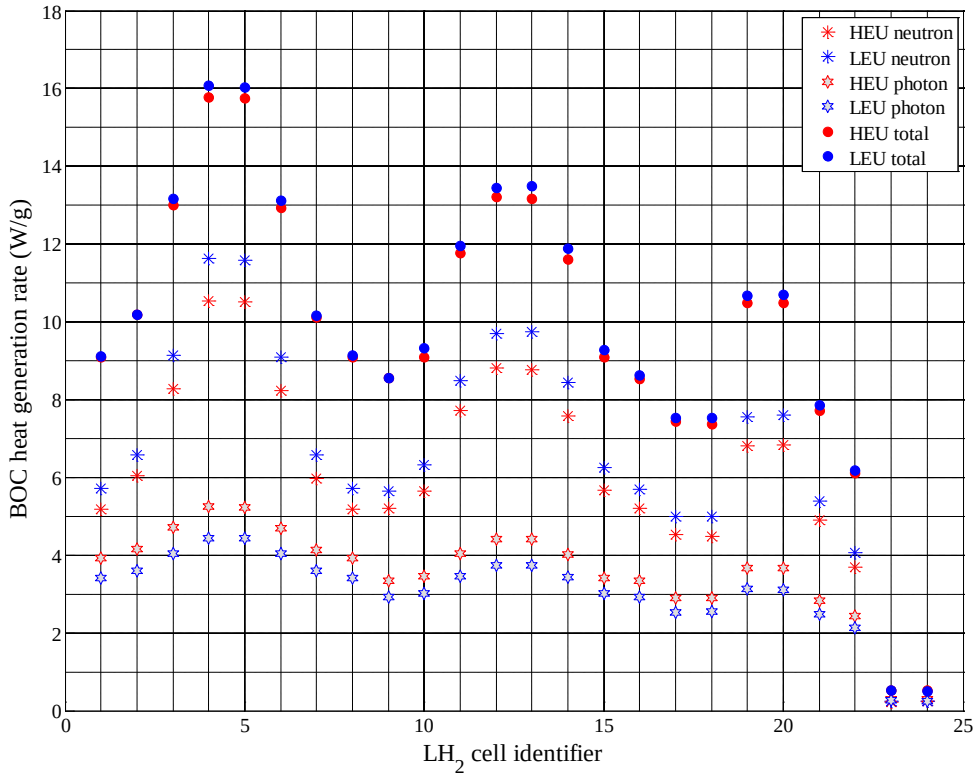

Fig. 5. Beginning-of-cycle heat generation rates in LH_2 sections 2–6.

Table 6. Beginning-of-cycle total heat generation rate summary for the cold source LH_2 regions

Cold source LH_2 region	Mass (g)	85 MW HEU		100 MW LEU		(LEU−HEU)/HEU (%)
		W[a]	avg. W/g[b]	W	avg. W/g	
hemispherical part	16.14	205.94	12.76	208.55	12.92	1.27
section 2	9.77	117.81	12.06	119.17	12.20	1.15
section 3	4.81	51.86	10.79	52.68	10.96	1.58
section 4	2.31	20.68	8.94	21.08	9.12	1.94
sections 5 & 6	32.24	21.13	0.66	21.02	0.65	−0.52
sum of above	65.27	417.43	6.40	422.50	6.47	1.21

[a] $W = \sum H_i M_i$, where H is heating rate (W/g), M is mass (g), and i = 1:N (N is the number of cells in the region of interest)
[b] avg. W/g is mass weighted: $H_{avg} = (\sum H_i M_i) / (\sum M_i)$

Table 7. Beginning-of-cycle radiation-dependent heat generation rate summary for the cold source LH_2 regions

Cold source LH_2 region	85 MW HEU		100 MW LEU		(LEU−HEU)/HEU	
	neutron	photon	neutron	photon	neutron (%)	photon (%)
hemispherical part (W[a])	126.34	79.60	139.90	68.64	10.73	−13.76
section 2 (W)	73.72	44.10	81.27	37.89	10.25	−14.07
section 3 (W)	33.33	18.53	36.76	15.92	10.28	−14.07
section 4 (W)	13.10	7.59	14.54	6.54	11.01	−13.72
sections 5 & 6 (W)	10.36	10.78	11.31	9.71	9.20	−9.87
sum of above (W)	256.84	160.59	283.78	138.72	10.49	−13.62
percent of total	61.53%	38.47%	67.26%	32.83%	9.16	−14.66
avg. W/g[b]	3.94	2.46	4.35	2.13	10.49	−13.62

[a] $W = \sum H_i M_i$, where H is heating rate (W/g), M is mass (g), and i = 1:N (N is the number of cells in the region of interest)
[b] avg. W/g is mass weighted: $H_{avg} = (\sum H_i M_i) / (\sum M_i)$

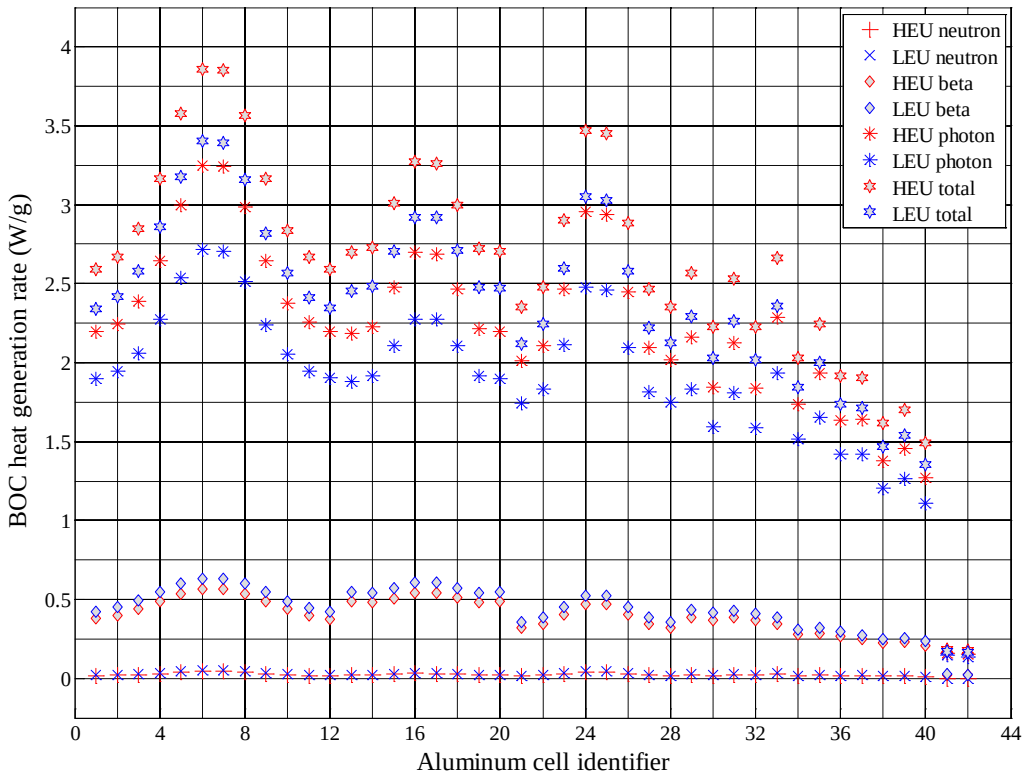

Fig. 6. Beginning-of-cycle heat generation rates in aluminum sections.

Table 8. Beginning-of-cycle total heat generation rate summary for the cold source aluminum regions

Cold source aluminum region	Mass (g)	85 MW HEU		100 MW LEU		(LEU−HEU)/HEU (%)
		W[a]	avg. W/g[b]	W	avg. W/g	
hemispherical part	73.66	229.48	3.12	205.50	2.79	−10.45
section 2	49.51	144.43	2.92	130.54	2.64	−9.62
section 3	79.16	221.09	2.79	197.62	2.50	−10.62
beyond section 3	547.88	593.75	1.08	535.66	0.98	−9.78
sum of above	750.20	1188.75	1.58	1069.32	1.43	−10.05

[a] $W = \sum H_i M_i$, where H is heating rate (W/g), M is mass (g), and i = 1:N (N is the number of cells in the region of interest)
[b] avg. W/g is mass weighted: $H_{avg} = (\sum H_i M_i) / (\sum M_i)$

Table 9. Beginning-of-cycle radiation-dependent heat generation rate summary for the cold source aluminum regions

Cold source aluminum region	85 MW HEU			100 MW LEU			(LEU−HEU)/HEU		
	neutron	photon	beta	neutron	photon	beta	neutron (%)	photon (%)	beta (%)
hemispherical part (W[a])	2.14	192.92	34.42	2.38	164.48	38.64	11.13	−14.74	12.27
section 2 (W)	1.22	118.20	25.01	1.35	101.15	28.04	10.13	−14.42	12.11
section 3 (W)	2.11	188.47	30.52	2.32	161.14	34.16	10.05	−14.50	11.95
beyond section 3 (W)	5.19	503.59	84.97	5.74	434.81	95.11	10.45	−13.66	11.94
sum of above (W)	10.67	1003.17	174.91	11.79	861.59	195.95	10.47	−14.11	12.03
percent of total	0.90%	84.39%	14.71%	1.10%	80.57%	18.32%	22.81	−4.52	24.54
avg. W/g[b]	0.01	1.34	0.23	0.02	1.15	0.26	10.47	−14.11	12.03

[a] $W = \sum H_i M_i$, where H is heating rate (W/g), M is mass (g), and i = 1:N (N is the number of cells in the region of interest)
[b] avg. W/g is mass weighted: $H_{avg} = (\sum H_i M_i) / (\sum M_i)$

4.3 END-OF-CYCLE HEAT GENERATION RESULTS

EOC specific nuclear heat generation rates are presented in this section. For both the HEU and LEU cases, the CEs are fully withdrawn. Thus, the aluminum only sections of the CEs are surrounding the fueled section of the core, and the neutron absorbing regions in the outer and inner control elements are respectively situated above and below the fueled section of the core.

The EOC neutron-induced, photon-induced, and total heat generation rates are illustrated in Fig. 7 for the cold source LH_2 hemispherical region and in Fig. 8 for sections 2–6 of the cold source LH_2. Both figures again show that neutron energy deposition is greater than photon energy deposition in the cold source LH_2 regions for both fuel types. For the EOC configuration, the neutron energy deposition rates are still greater for the LEU core and the photon energy deposition rates are still greater for the HEU core, but the total heat generation rates for the LH_2 regions are now slightly greater for the HEU core.

As shown in Table 10, the average EOC total heat generation rates in the hemispherical region of the cold source LH_2 for the HEU and LEU cores are 13.25 and 12.86 W/g, respectively. Thus, the EOC heat generation rate in the cold source hemisphere LH_2 is about 3.0% greater for the HEU core compared to the LEU core. The total estimated energy deposition in the 65.27 grams of LH_2 in the regions tallied on is 432.8 and 420.3 watts, respectively, for the HEU and LEU cores at EOC.

From BOC to EOC, the total heat generation rate in the cold source hemisphere LH_2 increased about 3.8% for the HEU core and decreased about 0.4% for the LEU core. The total energy deposition in the LH_2 regions increased about 3.7% for the HEU core and decreased about 0.5% for the LEU core from BOC to EOC.

A comparison of the radiation-dependent LH_2 heat generation rates for the HEU core and the LEU core is provided in Table 11. As shown in this table, the neutron-induced heat generation rates contribute about 58.3% and 65.4%, respectively, to the total heat generation rate in the LH_2 regions for the HEU and LEU cores, and thus photon-induced heat generation rates contribute about 41.7% and 34.6%, respectively, to the total heat generation rate in the LH_2 regions for the HEU and LEU cores. The neutron-induced heat generation rates in the cold source LH_2 regions for both cores decreased a small amount from BOC to EOC (about 2% and 3%, respectively, for the HEU and LEU cores); however, the photon-induced heat generation rates in the LH_2 regions for the HEU and LEU cores increased about 5% and 12%,

respectively. This large increase in the photon energy deposition rates in the HEU core causes the LH_2 total energy deposition to be slightly greater for the HEU core compared to the LEU core at EOC.

As shown in Fig. 9, the EOC total heat generation rates in the cold source aluminum regions are greater when the HEU core is operating than when the reference LEU core is. As described in Section 4.2, photon energy deposition is the dominant heating mechanism in aluminum and neutron energy deposition is a negligible factor.

Table 12 provides a summary of heat generation rates in the cold source aluminum regions, and Table 13 provides a summary of the radiation-dependent heat generation rates. As shown in these tables, the total heat generation rates in the cold source aluminum regions are about 17% lower for the LEU core in comparison to the HEU core under EOC conditions. The total heat generation rates in these regions increased by about 14% and 5%, respectively, for the HEU and LEU cores from BOC to EOC. At EOC, beta-induced energy deposition rates due to the LEU core are estimated to be about 2%–3% greater than those due to the HEU core, but the photon-induced energy deposition rates due to the LEU core are estimated to be about 20%–21% lower than those due to the HEU core.

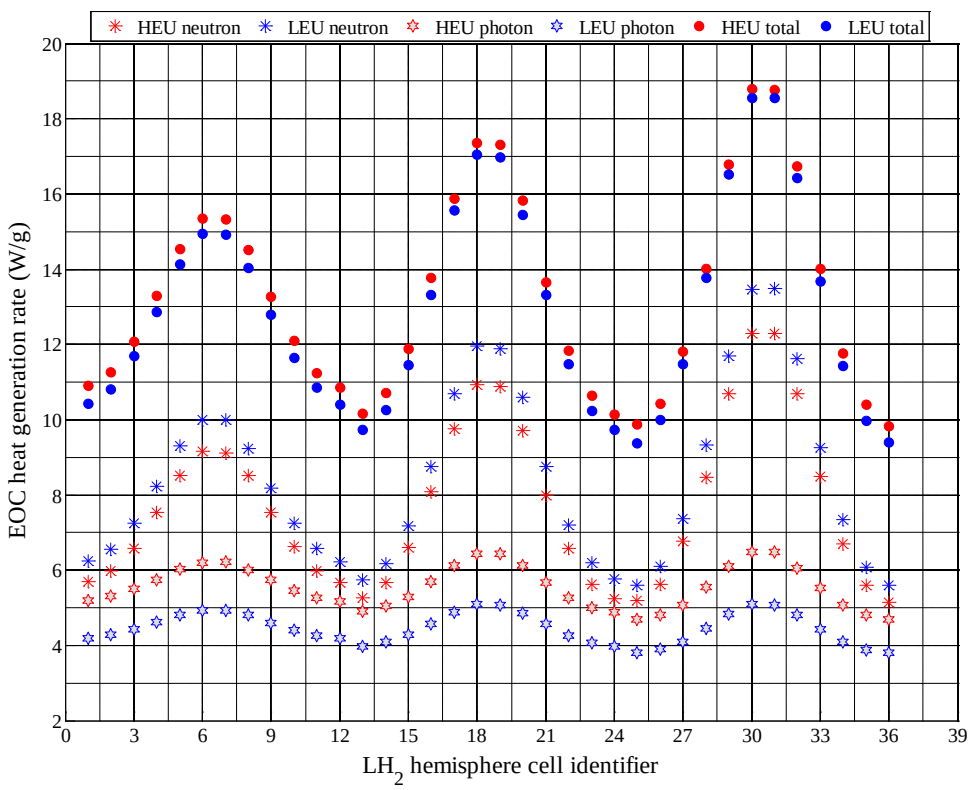

Fig. 7. End-of-cycle heat generation rates in LH_2 hemisphere.

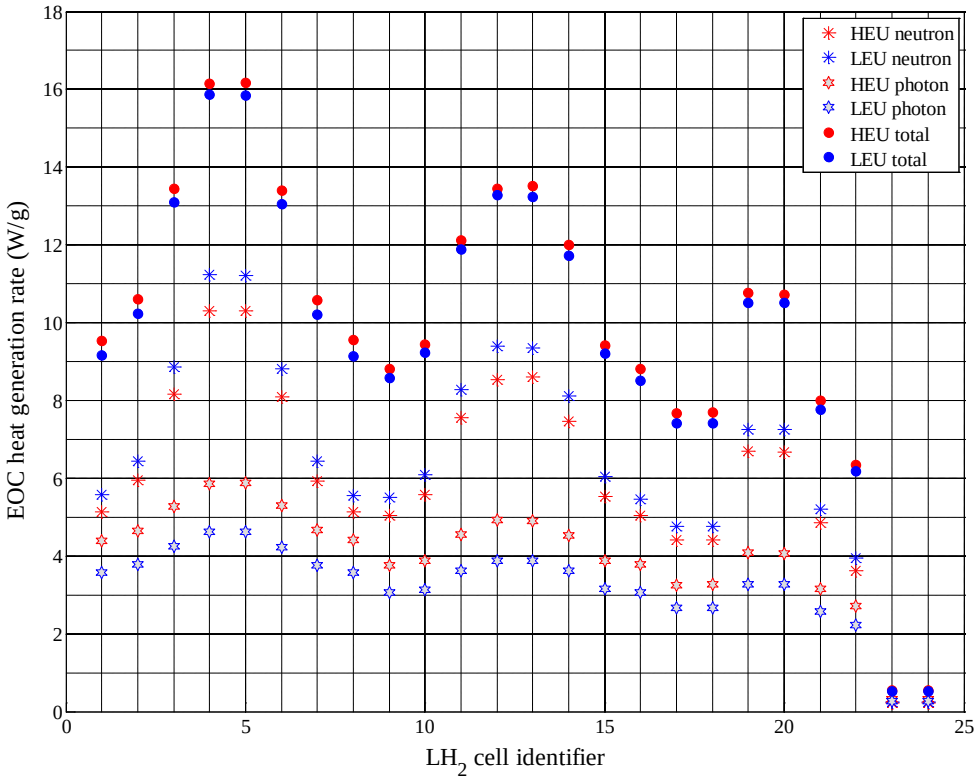

Fig. 8. End-of-cycle heat generation rates in LH_2 sections 2–6.

Table 10. End-of-cycle total heat generation rate summary for the cold source LH_2 regions

Cold source LH_2 region	Mass (g)	85 MW HEU		100 MW LEU		(LEU−HEU)/HEU (%)
		W[a]	avg. W/g[b]	W	avg. W/g	
hemispherical part	16.14	213.86	13.25	207.63	12.86	−2.91
section 2	9.77	122.07	12.50	118.59	12.14	−2.84
section 3	4.81	53.27	11.08	52.09	10.83	−2.21
section 4	2.31	21.31	9.22	20.75	8.97	−2.66
sections 5 & 6	32.24	22.29	0.69	21.29	0.66	−4.50
sum of above	65.27	432.79	6.63	420.35	6.44	−2.87

[a] $W = \sum H_i M_i$, where H is heating rate (W/g), M is mass (g), and i = 1:N (N is the number of cells in the region of interest)
[b] avg. W/g is mass weighted: $H_{avg} = (\sum H_i M_i) / (\sum M_i)$

Table 11. End-of-cycle radiation-dependent heat generation rate summary for the cold source LH_2 regions

Cold source LH_2 region	85 MW HEU		100 MW LEU		(LEU−HEU)/HEU	
	neutron	photon	neutron	photon	neutron (%)	photon (%)
hemispherical part (W[a])	124.18	89.68	135.70	71.93	9.28	−19.78
section 2 (W)	72.58	49.49	78.91	39.68	8.73	−19.82
section 3 (W)	32.51	20.76	35.46	16.63	9.09	−19.91
section 4 (W)	12.83	8.49	13.89	6.86	8.29	−19.21
sections 5 & 6 (W)	10.13	12.16	11.00	10.29	8.54	−15.37
sum of above (W)	252.22	180.57	274.96	145.39	9.02	−19.48
percent of total	58.28%	41.72%	65.41%	34.59%	12.24	−17.10
avg. W/g[b]	3.86	2.77	4.21	2.23	9.02	−19.48

[a] $W = \sum H_i M_i$, where H is heating rate (W/g), M is mass (g), and i = 1:N (N is the number of cells in the region of interest)
[b] avg. W/g is mass weighted: $H_{avg} = (\sum H_i M_i) / (\sum M_i)$

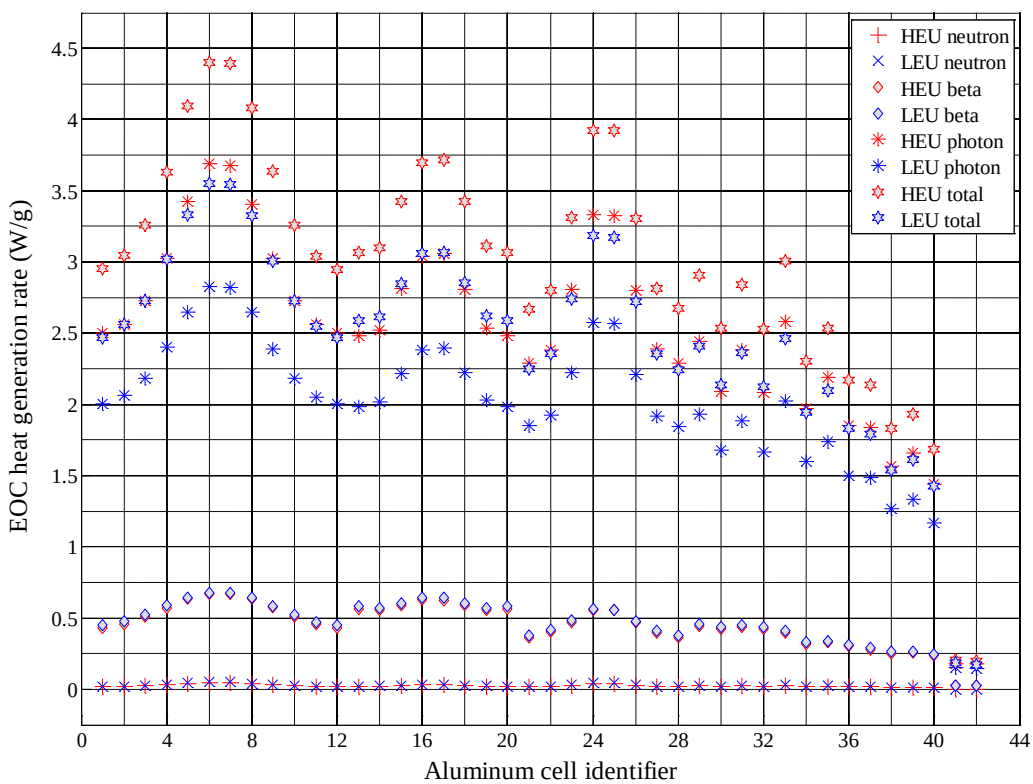

Fig. 9. End-of-cycle heat generation rates in aluminum sections.

Table 12. End-of-cycle total heat generation rate summary for the cold source aluminum regions

Cold source aluminum region	Mass (g)	85 MW HEU		100 MW LEU		(LEU−HEU)/HEU (%)
		W[a]	avg. W/g[b]	W	avg. W/g	
hemispherical part	73.66	262.44	3.56	216.68	2.94	−17.44
section 2	49.51	164.24	3.32	137.39	2.78	−16.35
section 3	79.16	251.56	3.18	208.00	2.63	−17.32
beyond section 3	547.88	672.50	1.23	563.05	1.03	−16.27
sum	750.20	1350.74	1.80	1125.12	1.50	−16.70

[a] $W = \sum H_i M_i$, where H is heating rate (W/g), M is mass (g), and i = 1:N (N is the number of cells in the region of interest)
[b] avg. W/g is mass weighted: $H_{avg} = (\sum H_i M_i) / (\sum M_i)$

Table 13. End-of-cycle radiation-dependent heat generation rate summary for the cold source aluminum regions

Cold source aluminum region	85 MW HEU			100 MW LEU			(LEU−HEU)/HEU		
	neutron	photon	beta	neutron	photon	beta	neutron (%)	photon (%)	beta (%)
hemispherical part (W[a])	2.12	220.01	40.31	2.31	173.25	41.12	9.06	−21.25	2.02
section 2 (W)	1.21	134.26	28.77	1.32	106.49	29.59	8.85	−20.69	2.84
section 3 (W)	2.07	213.96	35.53	2.26	169.48	36.26	8.98	−20.79	2.04
beyond section 3 (W)	5.07	570.18	97.24	5.54	457.22	100.29	9.26	−19.81	3.14
sum of above (W)	10.47	1138.41	201.85	11.43	906.43	207.26	9.12	−20.38	2.68
percent of total	0.78%	84.28%	14.94%	1.02%	80.56%	18.42%	31.00	−4.41	23.27
avg. W/g[b]	0.01	1.52	0.27	0.02	1.21	0.28	9.12	−20.38	2.68

[a] $W = \sum H_i M_i$, where H is heating rate (W/g), M is mass (g), and i = 1:N (N is the number of cells in the region of interest)
[b] avg. W/g is mass weighted: $H_{avg} = (\sum H_i M_i) / (\sum M_i)$

4.4 FITS TO HEAT GENERATION RATES

Various mathematic functions were generated to fit the spatially dependent specific nuclear heat generation rates in the cold source LH_2 moderator and vessel regions. The basis functions of the fitting functions are those generated in [2] and [4]. The coefficients are determined with linear least square methods and MATLAB scripts developed during this project. Fitting coefficients were generated for the neutron-induced, beta-induced (aluminum only), photon-induced, and total energy deposition in the regions described previously. The coefficients calculated for the total heat generation rates in the LH_2 hemispherical region for both cores at BOC and EOC are listed in Table 14. The radiation-dependent fitting functions for the LH_2 hemispherical region and the fitting functions for the other cold source LH_2 regions can be found in [5].

The total calculated and fitted heat generation rates in the LH_2 hemispherical region for both cores at BOC and EOC and the percent differences between the calculated and fitted values are provided in Table 15. As shown in this table, the fitted values are in good agreement with the calculated results; the differences range from −0.5% to +0.7%. The fitted neutron, photon, and combined neutron + photon (i.e., total) heat generation rates in the LH_2 hemispherical region for the BOC HEU and LEU cores are illustrated in Fig. 10–Fig. 12. Fig. 13–Fig. 15 show the EOC fitted neutron, photon, and total heat

generation rates. For each set of surface plots, the color maps have the same axes to allow a visual comparison between the HEU and LEU results.

Table 14. Fitting coefficients to total heat generation rates in hemispherical part of cold source LH_2

Coef.	Function[a]	BOC HEU	BOC LEU	EOC HEU	EOC LEU
C_1	1	1.20506E+01	1.25040E+01	1.29235E+01	1.25343E+01
C_2	$r\cos(\theta)$	−8.24578E−01	−8.64197E−01	−8.40474E−01	−8.28626E−01
C_3	$r\sin(\theta)$	7.67442E−03	1.65974E−02	9.35677E−03	8.97120E−03
C_4	$r\sin(\theta)\cos(\theta)$	−7.17075E−04	2.39634E−02	−9.13475E−03	−2.85415E−02
C_5	$r^2\cos(2\theta)$	5.32530E−02	5.86452E−02	4.99830E−02	4.59048E−02
C_6	$r^2\sin(2\theta)$	3.94907E−04	−4.87006E−03	1.24248E−03	2.30816E−03
C_7	$r^2\sin(2\theta)\cos(2\theta)$	3.99418E−04	−3.76982E−04	2.85073E−04	1.38062E−04
C_8	r	−5.19770E−02	−2.94708E−01	−2.44958E−01	−3.03355E−01
C_9	r^2	6.76885E−02	1.10943E−01	9.06477E−02	1.06672E−01
C_{10}	$r\cos(2\theta)$	−4.82783E−02	−5.38916E−02	−3.49317E−02	−1.93906E−02
C_{11}	$r^3\cos(\theta)\cos(2\theta)$	−1.23536E−02	−1.41739E−02	−1.13688E−02	−1.34126E−02
C_{12}	$r^3\cos(\theta)\sin(2\theta)$	6.74187E−05	−6.26712E−04	−4.67653E−05	−9.22994E−05
C_{13}	$r^3\sin(\theta)\cos(2\theta)$	−3.11552E−05	−1.45394E−04	2.52584E−04	2.30219E−04
C_{14}	$r^3\sin(\theta)\sin(2\theta)$	−1.03066E−02	−1.13080E−02	−9.54375E−03	−1.13191E−02

[a] r is the radius (cm) and θ is the angle (radians)

Table 15. Fits to total heat generation rates in hemispherical part of cold source LH_2

Identifier	Cell	BOC HEU			BOC LEU			EOC HEU			EOC LEU		
		input (W/g)	fit (W/g)	diff. (%)	input (W/g)	fit (W/g)	diff. (%)	input (W/g)	fit (W/g)	diff. (%)	input (W/g)	fit (W/g)	diff. (%)
1	95001	10.36	10.32	−0.36	10.38	10.33	−0.48	10.89	10.84	−0.52	10.44	10.40	−0.35
2	95002	10.77	10.76	−0.12	10.81	10.79	−0.19	11.27	11.26	−0.10	10.82	10.81	−0.08
3	95003	11.61	11.60	−0.07	11.71	11.69	−0.11	12.08	12.11	0.20	11.69	11.65	−0.33
4	95004	12.74	12.77	0.29	12.90	12.92	0.15	13.29	13.30	0.10	12.85	12.86	0.07
5	95005	13.99	14.00	0.06	14.23	14.21	−0.11	14.54	14.56	0.10	14.12	14.14	0.12
6	95006	14.80	14.81	0.09	15.05	15.08	0.16	15.35	15.38	0.16	14.94	14.97	0.17
7	95007	14.78	14.81	0.18	15.04	15.06	0.18	15.32	15.36	0.32	14.93	14.94	0.07
8	95008	13.97	13.98	0.02	14.15	14.16	0.08	14.52	14.52	−0.01	14.03	14.07	0.27
9	95009	12.70	12.73	0.24	12.81	12.84	0.23	13.27	13.26	−0.08	12.79	12.80	0.09
10	95010	11.57	11.56	−0.11	11.59	11.61	0.12	12.09	12.07	−0.13	11.64	11.64	−0.02
11	95011	10.75	10.72	−0.21	10.77	10.75	−0.16	11.24	11.24	−0.04	10.85	10.82	−0.24
12	95012	10.33	10.31	−0.23	10.33	10.32	−0.07	10.85	10.82	−0.22	10.41	10.41	0.02
13	95013	9.69	9.73	0.40	9.61	9.67	0.68	10.16	10.20	0.36	9.72	9.74	0.23
14	95014	10.25	10.28	0.28	10.21	10.26	0.53	10.71	10.74	0.29	10.25	10.29	0.38
15	95015	11.44	11.43	−0.09	11.52	11.52	0.02	11.88	11.89	0.09	11.45	11.48	0.28
16	95016	13.26	13.24	−0.16	13.43	13.43	−0.02	13.76	13.71	−0.34	13.32	13.35	0.23
17	95017	15.38	15.34	−0.23	15.69	15.66	−0.23	15.88	15.83	−0.29	15.56	15.50	−0.36
18	95018	16.86	16.82	−0.23	17.24	17.25	0.10	17.36	17.31	−0.27	17.04	17.00	−0.25
19	95019	16.82	16.81	−0.02	17.26	17.23	−0.19	17.31	17.30	−0.10	16.97	16.96	−0.09
20	95020	15.34	15.31	−0.20	15.63	15.57	−0.39	15.83	15.79	−0.24	15.46	15.42	−0.26
22	95021	13.21	13.18	−0.22	13.32	13.29	−0.27	13.65	13.67	0.15	13.31	13.28	−0.23
22	95022	11.37	11.38	0.01	11.41	11.41	0.06	11.85	11.85	−0.01	11.47	11.46	−0.08
23	95023	10.20	10.23	0.31	10.26	10.26	0.01	10.63	10.69	0.53	10.24	10.30	0.51
24	95024	9.64	9.71	0.69	9.68	9.70	0.22	10.13	10.17	0.40	9.73	9.75	0.17
25	95025	9.39	9.36	−0.26	9.31	9.29	−0.19	9.87	9.84	−0.31	9.38	9.36	−0.21
26	95026	9.98	9.98	0.03	9.99	9.96	−0.28	10.42	10.44	0.17	9.99	10.01	0.20
27	95027	11.33	11.33	0.01	11.47	11.45	−0.11	11.82	11.78	−0.34	11.47	11.43	−0.40
28	95028	13.59	13.59	−0.04	13.82	13.85	0.17	14.01	14.05	0.26	13.77	13.75	−0.11
29	95029	16.30	16.34	0.25	16.78	16.78	−0.04	16.78	16.81	0.18	16.52	16.56	0.26
30	95030	18.34	18.34	0.02	18.93	18.95	0.08	18.78	18.80	0.08	18.56	18.58	0.10
31	95031	18.33	18.33	−0.01	18.93	18.92	−0.05	18.78	18.78	0.02	18.56	18.54	−0.09
32	95032	16.27	16.29	0.14	16.62	16.67	0.27	16.74	16.77	0.13	16.44	16.48	0.28
33	95033	13.50	13.51	0.11	13.64	13.66	0.14	14.01	14.01	−0.02	13.67	13.69	0.11
34	95034	11.28	11.26	−0.13	11.36	11.34	−0.19	11.76	11.74	−0.11	11.44	11.41	−0.30
35	95035	9.91	9.91	0.08	9.99	10.01	0.24	10.40	10.38	−0.14	9.97	10.00	0.30
36	95036	9.37	9.33	−0.50	9.39	9.36	−0.34	9.82	9.80	−0.23	9.40	9.36	−0.45

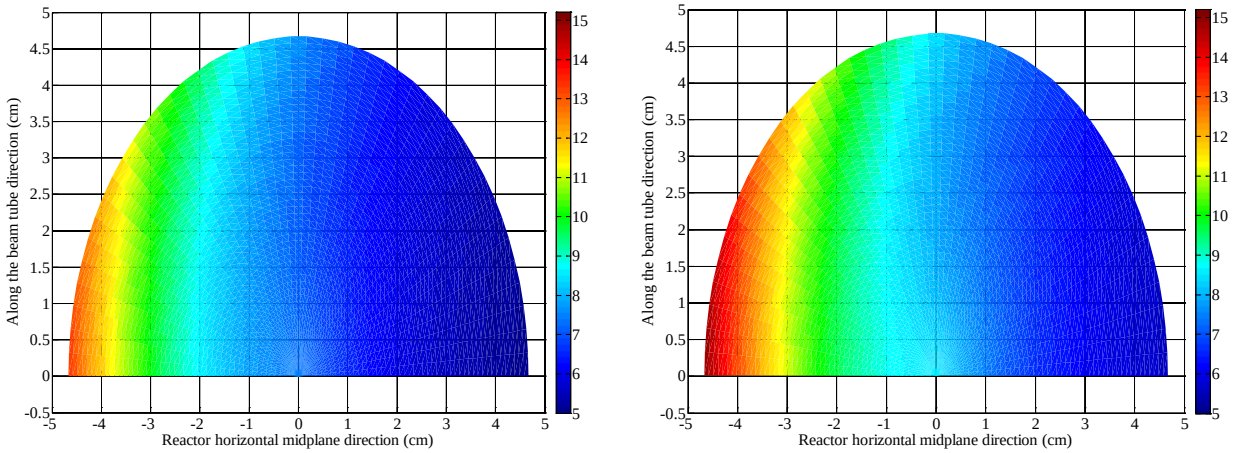

(a) (b)

Fig. 10. Beginning-of-cycle LH_2 hemisphere neutron energy deposition (W/g): HEU (a) and LEU (b).

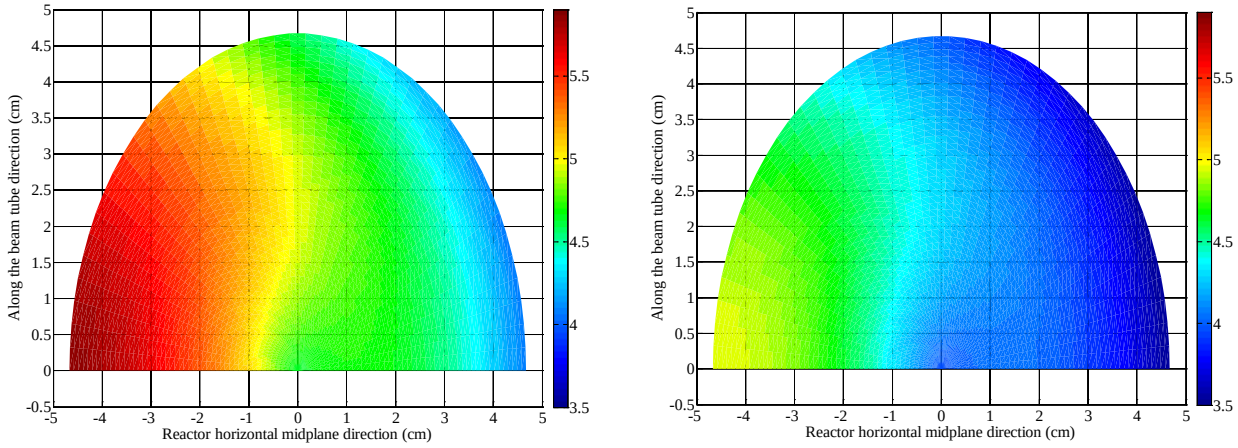

(a) (b)

Fig. 11. Beginning-of-cycle LH_2 hemisphere photon energy deposition (W/g): HEU (a) and LEU (b).

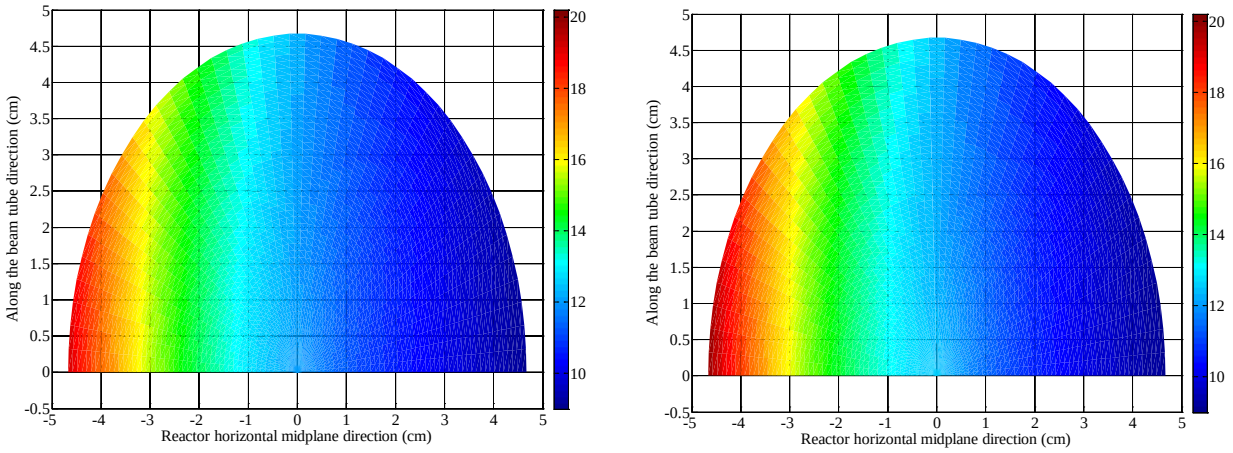

(a) (b)

Fig. 12. Beginning-of-cycle LH_2 hemisphere total energy deposition (W/g): HEU (a) and LEU (b).

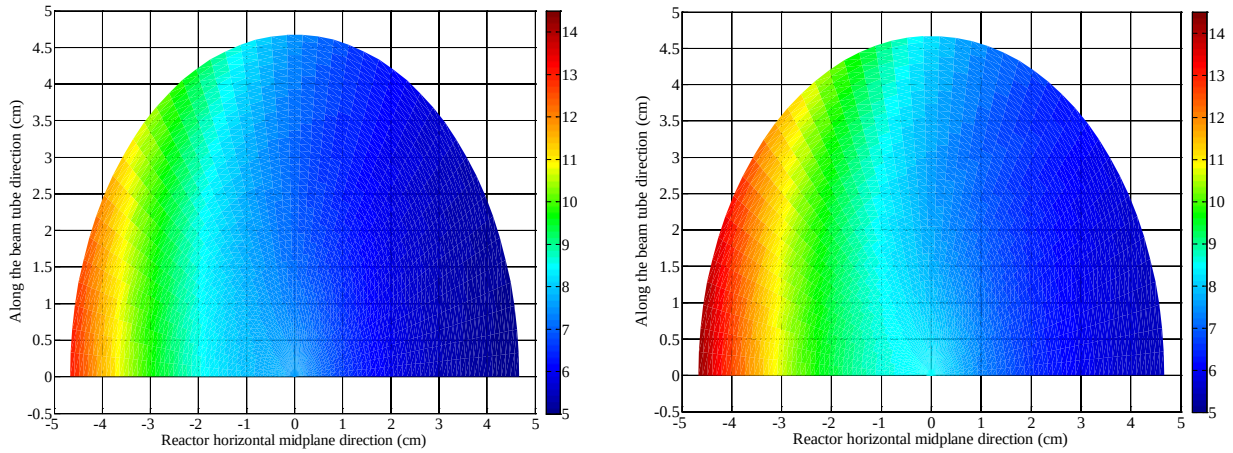

(a) (b)

Fig. 13. End-of-cycle LH_2 hemisphere neutron energy deposition (W/g): HEU (a) and LEU (b).

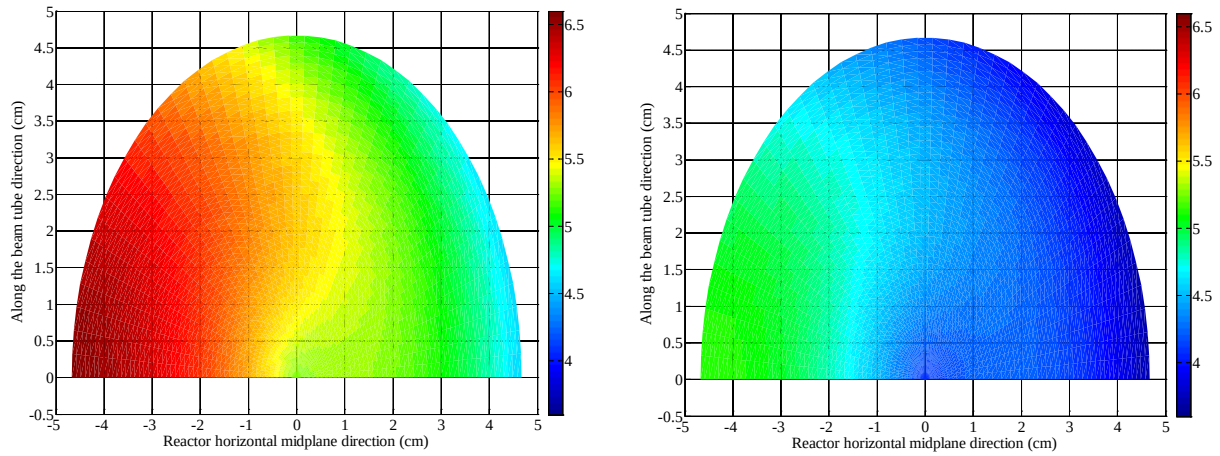

(a) (b)

Fig. 14. End-of-cycle LH_2 hemisphere photon energy deposition (W/g): HEU (a) and LEU (b).

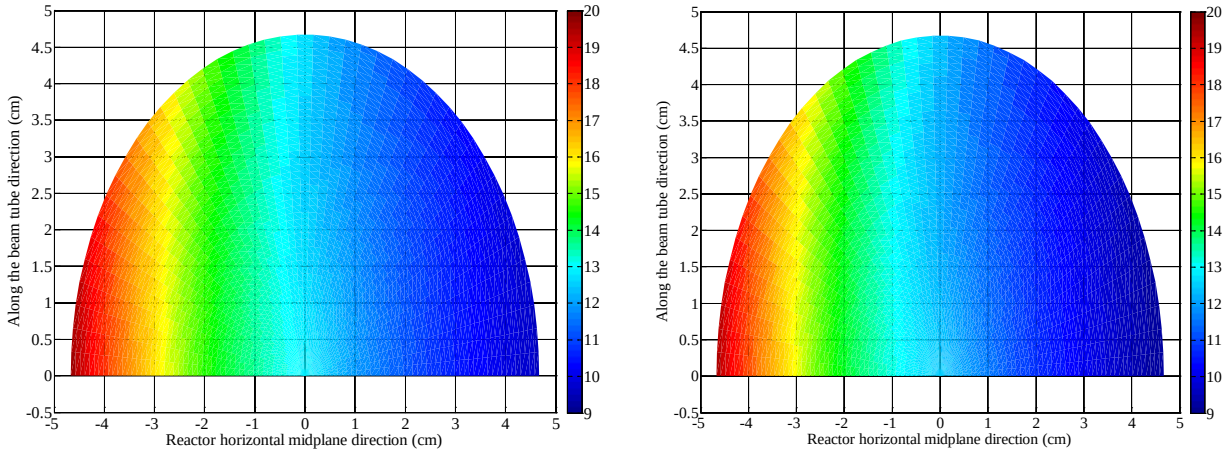

(a) (b)

Fig. 15. End-of-cycle LH_2 hemisphere total energy deposition (W/g): HEU (a) and LEU (b).

Table 16 gives the coefficients calculated for the total heat generation rates in the aluminum hemispherical region (i.e., neutron + photon + beta) for both cores at BOC and EOC. The radiation-dependent fitting functions for the aluminum hemispherical region and the fitting functions for the other cold source aluminum regions are provided in [5]. Table 17 provides the total calculated and fitted heat generation rates in the aluminum hemispherical region cells for both cores at BOC and EOC and the percent differences between the calculated and fitted values. As shown in this table, the fitted values are in good agreement with the calculated results; the differences range from −0.5% to +0.5%.

The ratios of the 85 MW HEU to the 100 MW LEU fitted neutron, beta, photon, and total heat generation rates in the aluminum hemispherical regions for the BOC and EOC cores are illustrated in Fig. 16 and Fig. 17.

Table 16. Fitting coefficients to total heat generation rates in hemispherical part of cold source aluminum

Coef.	Function[a]	BOC HEU	BOC LEU	EOC HEU	EOC LEU
C_1	1	3.11551E+00	2.79000E+00	3.56305E+00	2.94182E+00
C_2	cos(θ)	−6.46324E−01	−5.40767E−01	−7.45061E−01	−5.54808E−01
C_3	sin(θ)	3.26857E−03	1.18782E−02	2.43827E−03	4.71038E−03
C_4	cos(2θ)	1.27782E−01	9.46634E−02	1.32611E−01	8.00474E−02
C_5	sin(2θ)	−2.35996E−03	−6.93006E−03	−2.34234E−03	−4.62251E−04

[a] θ is the angle (radians)

Table 17. Fit to total heat generation rates in hemispherical part of cold source aluminum

Identifier	Cell	BOC HEU			BOC LEU			EOC HEU			EOC LEU		
		input (W/g)	fit (W/g)	diff. (%)	input (W/g)	fit (W/g)	diff. (%)	input (W/g)	fit (W/g)	diff. (%)	input (W/g)	fit (W/g)	diff. (%)
1	86021	2.59	2.60	0.32	2.34	2.35	0.39	2.95	2.96	0.13	2.47	2.48	0.20
2	86022	2.67	2.66	−0.31	2.42	2.41	−0.31	3.04	3.04	−0.27	2.56	2.55	−0.33
3	86023	2.85	2.84	−0.31	2.58	2.58	−0.15	3.26	3.26	−0.17	2.73	2.73	0.10
4	86024	3.16	3.18	0.39	2.86	2.86	0.05	3.63	3.64	0.37	3.02	3.02	0.02
5	86025	3.58	3.58	0.04	3.18	3.19	0.26	4.10	4.09	−0.07	3.33	3.34	0.10
6	86026	3.86	3.85	−0.15	3.40	3.40	−0.12	4.40	4.40	−0.12	3.55	3.55	−0.12
7	86027	3.85	3.85	−0.09	3.39	3.39	−0.16	4.40	4.40	−0.04	3.55	3.55	−0.03
8	86028	3.56	3.57	0.11	3.16	3.16	−0.06	4.08	4.09	0.14	3.33	3.33	0.05
9	86029	3.16	3.17	0.15	2.82	2.83	0.52	3.64	3.64	0.07	3.01	3.01	0.17
10	86030	2.84	2.84	−0.01	2.57	2.56	−0.32	3.26	3.25	−0.14	2.73	2.72	−0.25
11	86031	2.67	2.66	−0.49	2.41	2.41	−0.30	3.04	3.04	−0.20	2.55	2.55	0.00
12	86032	2.59	2.60	0.35	2.35	2.35	0.19	2.95	2.96	0.30	2.47	2.47	0.09

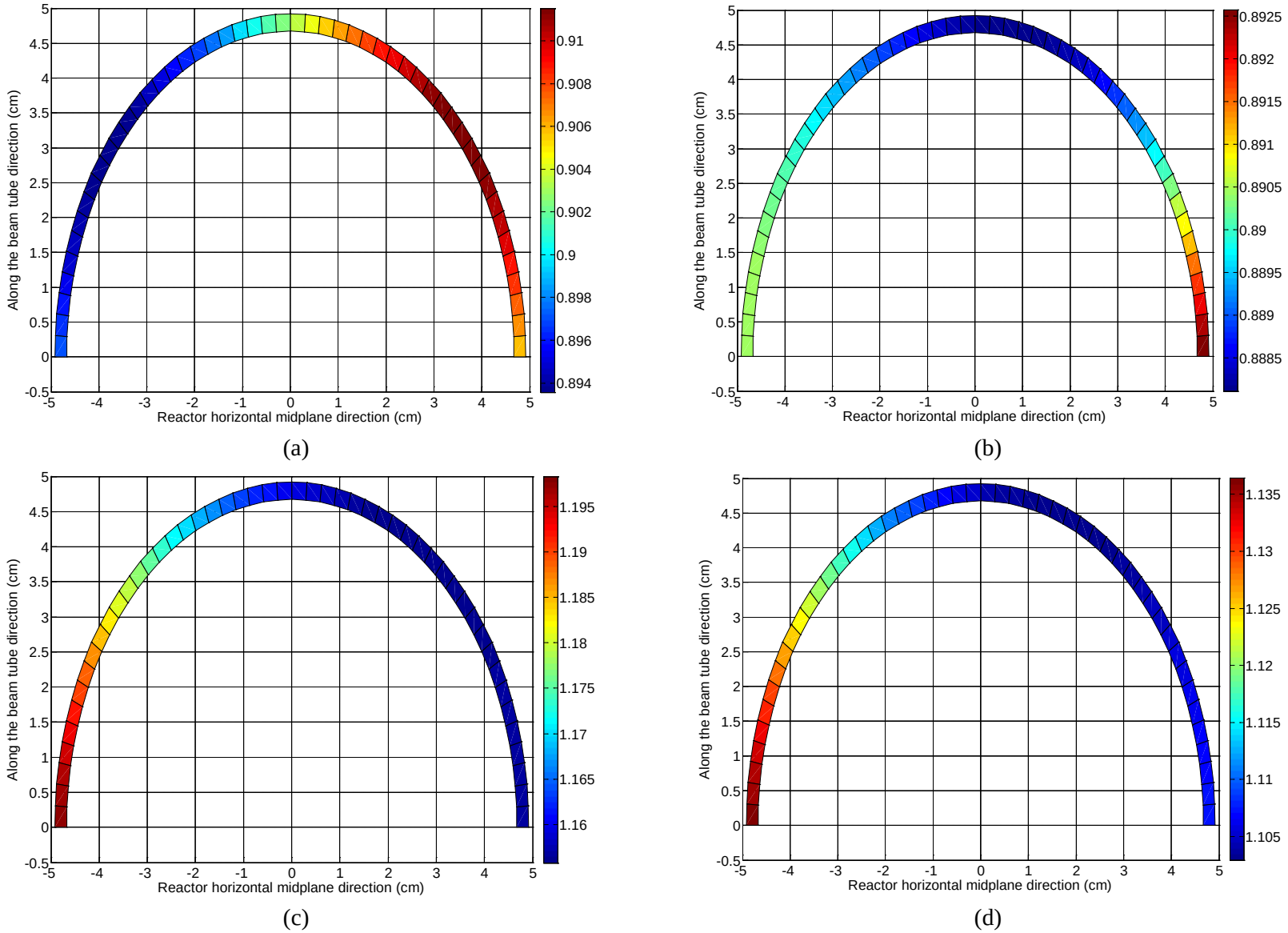

Fig. 16. Beginning-of-cycle aluminum hemisphere 85 HEU to 100 LEU ratio: neutron (a), beta (b), photon (c), and total (d).

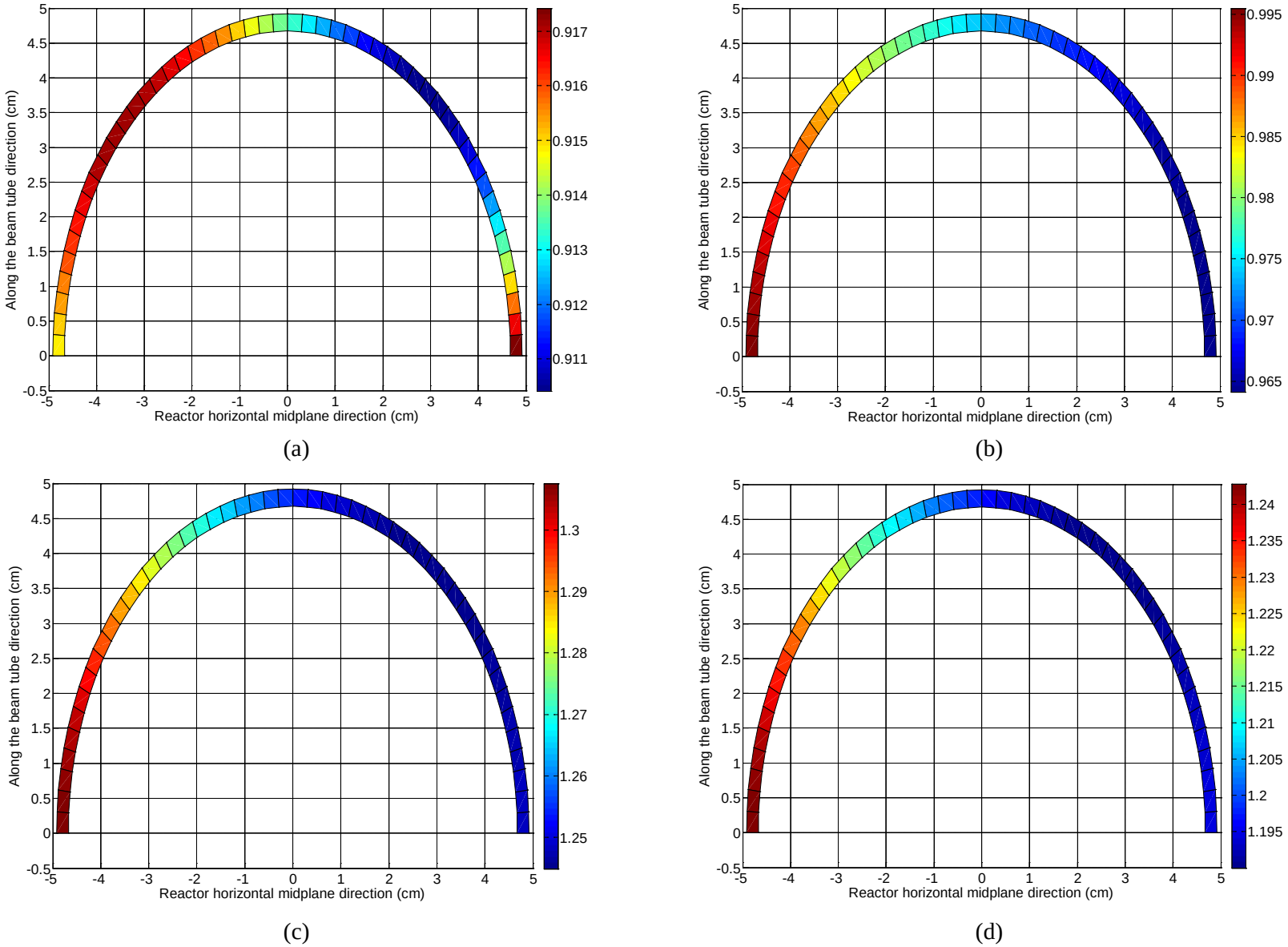

Fig. 17. End-of-cycle aluminum hemisphere 85 HEU to 100 LEU ratio: neutron (a), beta (b), photon (c), and total (d).

4.5 SILICON PRODUCTION RATE RESULTS

Silicon production rates in units of atoms of ^{28}Si per gram ^{27}Al per second were estimated for the cold source aluminum regions previously described (Table 3 and Table 4). Production rates at BOC and EOC are illustrated in Fig. 18 and Fig. 19. Production rates in cells 86157 and 86158 (i.e., identifiers 41 and 42) are not shown in these figures because their production rates are much lower than those of the other cells due to their location with respect to the fuel. For both BOC and EOC, the production rates for the reference LEU core are greater than those for the HEU core. The silicon production rate is dependent on the neutron flux (both magnitude and spectra), and because the thermal (and total) neutron flux in these aluminum regions increases over the course of the cycle for both core configurations, the EOC production rates are greater than those at BOC.

For the 40 cold source aluminum cells displayed in these figures, the HEU BOC production rates range from about 1.1×10^{12} to about 2.8×10^{12} $(g\text{-}s)^{-1}$, and the LEU BOC rates range from about 1.2×10^{12} to about 3.2×10^{12} $(g\text{-}s)^{-1}$. The BOC volume-averaged production rate for these regions is about 12.0% greater when the reactor is operating with the reference LEU core than when operating with the HEU core. However, the EOC volume-averaged production rate due to the LEU core is only about 2.7% greater than that due to the HEU core.

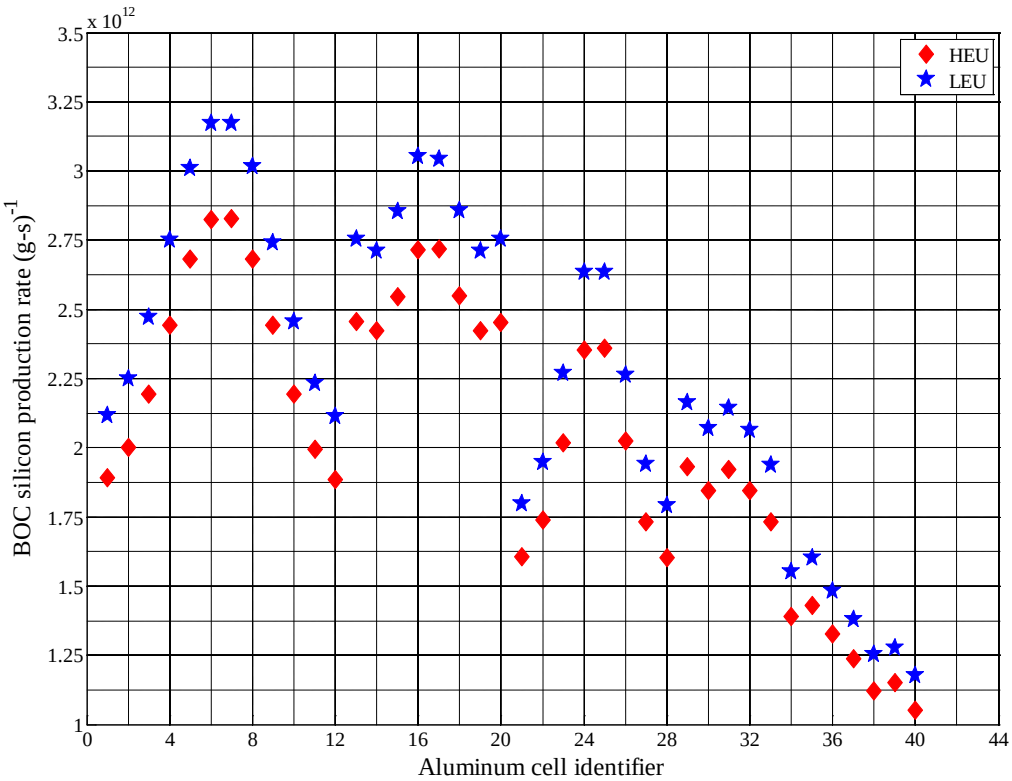

Fig. 18. Beginning-of-cycle silicon production rates in aluminum sections.

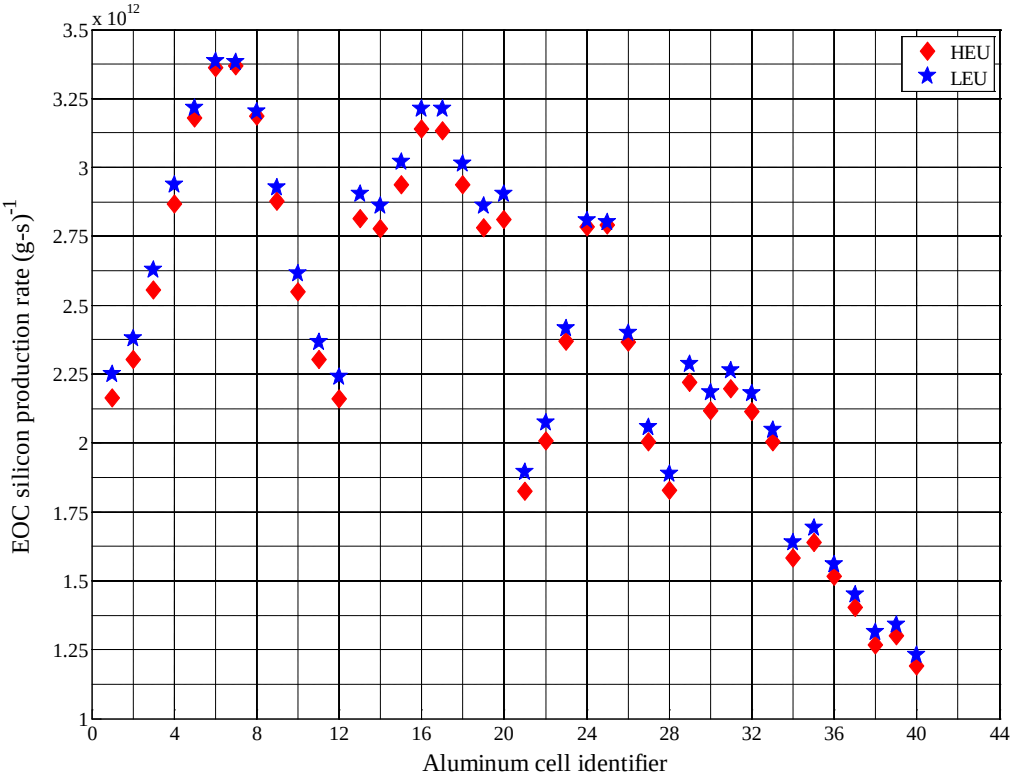

Fig. 19. End-of-cycle silicon production rates in aluminum sections.

4.6 NEUTRON FLUX IN LH_2 HEMISPHERE RESULTS

The impact of the HEU to LEU fuel conversion on the few-group neutron fluxes in the cold source LH_2 hemispherical region is discussed in this section. A previous study [7] was performed to assess the impact of the conversion on neutron fluxes at relevant experiment locations in the flux trap, beryllium reflector, and horizontal beam tubes. The study concluded that the BOC thermal, epithermal, and fast fluxes in a tally sphere placed in the HB-4 LH_2 region are about 12.21 ± 0.19%, 13.32 ± 0.37%, and 10.93 ± 0.53%, respectively, greater for the LEU core. At EOC, [7] concluded the thermal, epithermal, and fast fluxes for the LEU core are about 4.31 ± 0.17%, 13.28 ± 0.37%, and 11.26 ± 0.55%, respectively, greater than for the HEU core.

For the studies performed and documented in this report, the same three-group energy structure as that used in [7] was used to calculate the neutron fluxes on the spatial grid described in the previous sections for the cold source LH_2 and aluminum regions. The neutron fluxes calculated in the cold source LH_2 hemispherical region are documented here. Thermal, epithermal, fast, and total neutron fluxes in the 36 cells composing the LH_2 hemispherical region in the MCNP input are illustrated for the HEU and LEU cores at BOC and EOC in Fig. 20–Fig. 23. Fractional standard deviations of 0.0010–0.0013, 0.0019–0.0030, and 0.0032–0.0050 (i.e., all less than or equal to 0.5%) were obtained for the thermal, epithermal, and fast energy bins.

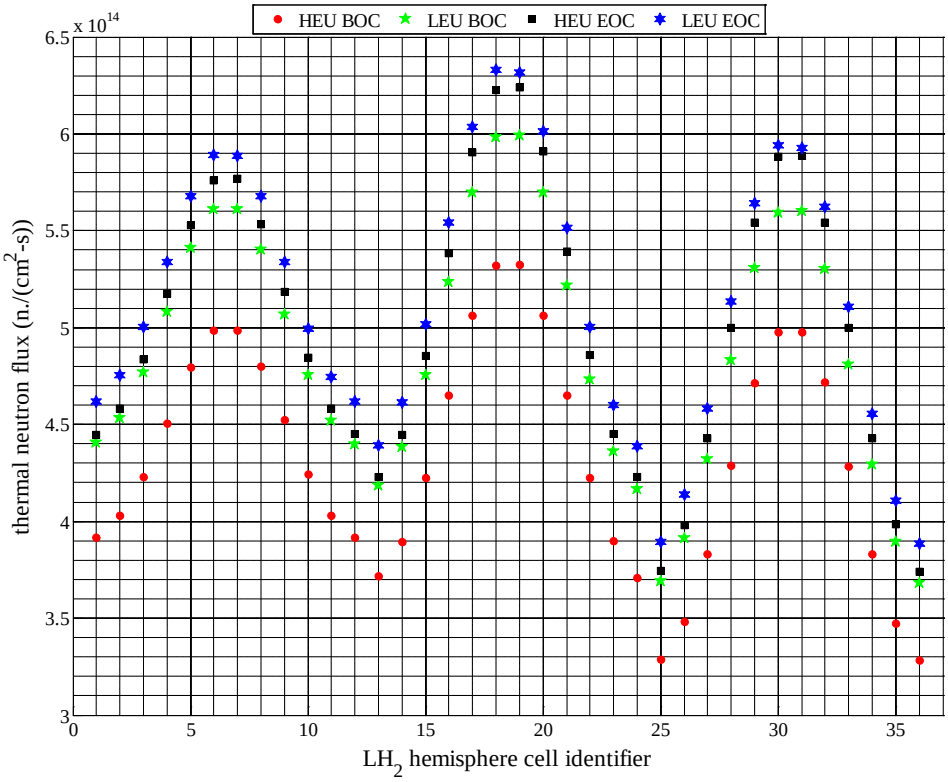

Fig. 20. Thermal (E_n < 0.625 eV) neutron flux in LH_2 hemisphere.

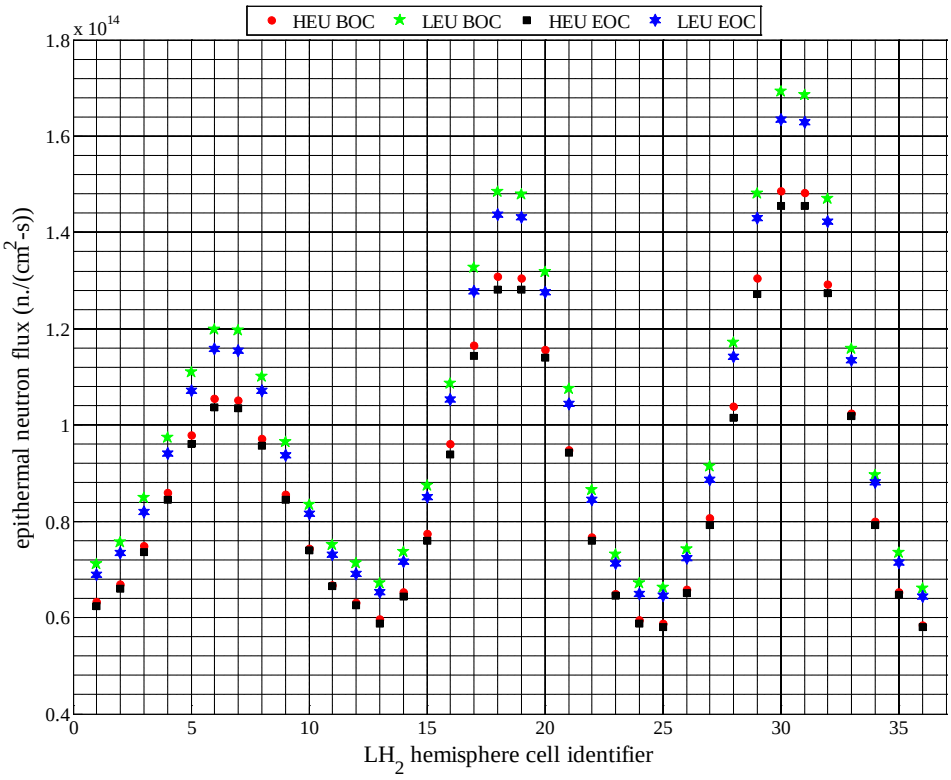

Fig. 21. Epithermal (0.1 MeV > E_n > 0.625 eV) neutron flux in LH_2 hemisphere.

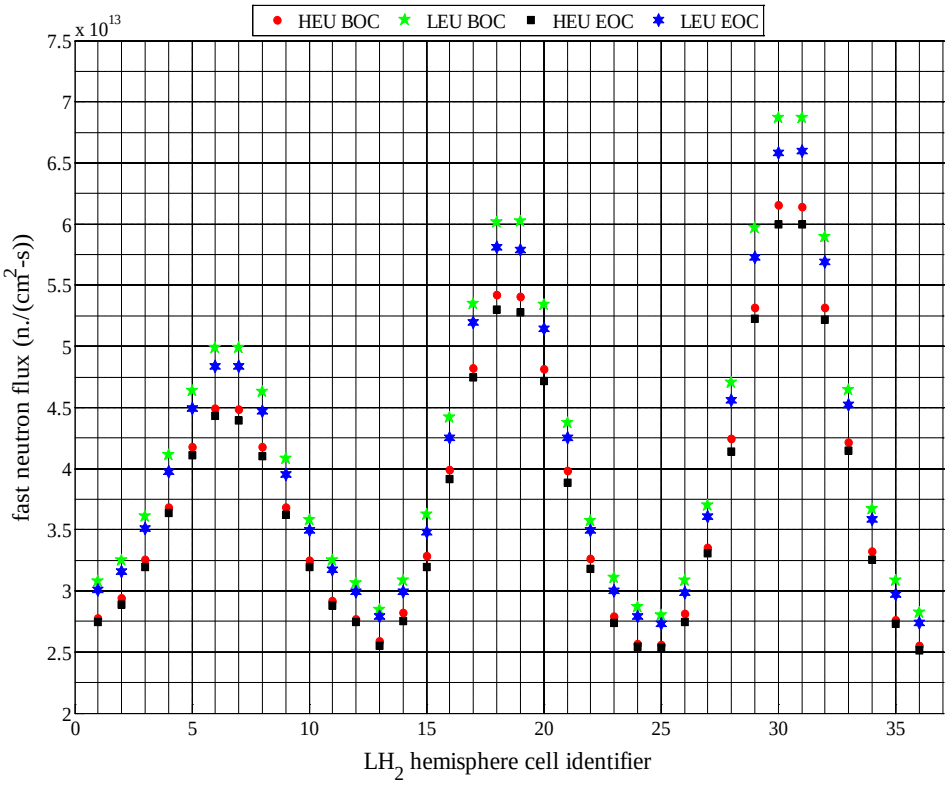

Fig. 22. Fast (20 MeV > E_n > 0.1 MeV) neutron flux in LH_2 hemisphere.

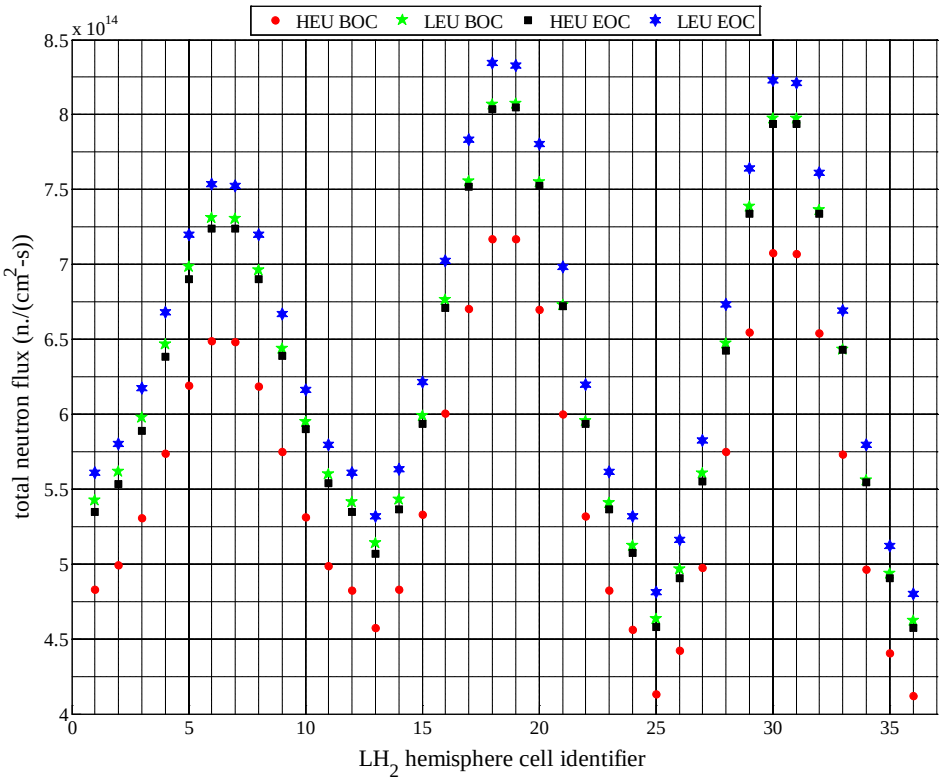

Fig. 23. Total neutron flux in LH_2 hemisphere.

As shown in Fig. 20, the thermal neutron flux is greatest for the LEU EOC core and increases from BOC to EOC for both the LEU and HEU cores. However, the percent increase from BOC to EOC is much greater for the HEU core, which is partly due to the CE positions described previously. The volume-averaged thermal flux for the HEU and LEU cores increased 15.5% and 5.5%, respectively, from BOC to EOC. At BOC, the volume-averaged thermal flux for the LEU core is about 12.4% greater than the HEU core, but at EOC, the thermal flux for the LEU core is only about 2.7% greater.

The epithermal and fast neutron fluxes actually decrease slightly from BOC to EOC for both the HEU and LEU cores. Under BOC conditions, the volume-averaged epithermal and fast fluxes were determined to be about 13.2% and 10.8% greater, respectively, for the LEU core. At EOC, the volume-averaged epithermal and fast fluxes in the LH_2 hemispherical region were determined to be about 11.5% and 9.4% greater, respectively, for the LEU core. The results compare well to those calculated in [7] when considering the Monte Carlo statistical uncertainties and the modeling differences.

5. SUMMARY AND CONCLUSIONS

As part of the HFIR HEU to LEU fuel conversion project, an assessment of the impact the conversion would have on nuclear heat generation rates, silicon production rates, and neutron fluxes in regions of the HFIR cold source has been performed. Neutronics calculations were performed with the MCNP5 computational tool and the HEU and reference LEU models documented in [1]. These models were modified as necessary to calculate detailed distributions of the heat generation rates, silicon production rates, and neutron fluxes. Calculations were performed with BOC and EOC conditions to bound typical irradiation conditions.

Volume-averaged BOC heat generation rates of 12.76 and 12.92 W/g, respectively, were calculated for the hemispherical region of the cold source LH_2 region for the HEU and LEU cores, and EOC heat generation rates of 13.25 and 12.86 W/g, respectively, were calculated for the HEU and LEU cores. Thus, the heat generation rates are slightly greater in the cold source moderator for the LEU core at BOC, but they are greater for the HEU core at EOC. The greatest heat generation rates in both the cold source LH_2 moderator and aluminum vessel were determined to occur at EOC for the HEU core. Therefore, the current heat removal system will retain its ability to remove the heat deposited in the cold source system.

As shown in Figure 3 of [2], the total heat deposition in the cold source moderator and vessel varies between about 2.0 and 2.2 kW during a typical cycle. The total heat depositions calculated in this report, based on the cycle 400 core configuration, for the 85 MW HEU core at BOC and EOC, are about 1.6 and 1.8 kW, respectively. Thus, the calculations based on the cycle 400 input are underestimating the total heat deposited in the cold source moderator and vessel during a typical cycle. This underestimation is primarily due to the beryllium reflector experiment loading modeled in the cycle 400 MCNP input (see Appendix). However, the purpose of this report is to assess the impact the conversion has on the heat generation rates, and because the beryllium reflector experiment loading is the same for both the HEU and LEU inputs, a fair comparison is made. Also, the BOC calculations are expected to be lower than measured results because a true BOC measurement is not possible due to the fuel composition changing in a shorter time span than that required for the measurements [2].

The thermal neutron flux ($E_n < 0.625$ eV) in the cold source LH_2 hemispherical region is greatest for the LEU EOC core and increases from BOC to EOC for both the LEU and HEU cores. The volume-averaged thermal flux in the hemisphere LH_2 for the HEU and LEU cores increased about 15.5% and 5.5%, respectively, from BOC to EOC. At BOC, the volume-averaged thermal flux for the LEU core is about 12.4% greater than that for the HEU core, but at EOC, the thermal flux for the LEU core is only about 2.7% greater. Because the thermal neutron flux in the cold source moderator is greater for the LEU core, the number of neutrons cooled by the LH_2 and transported to the scattering instruments located in the cold guide hall will also be enhanced. Thus, cold neutron scattering will not be adversely affected by the HEU to LEU fuel conversion.

Similar trends to those observed in the thermal flux results were observed in the silicon production rate results since they are dependent on the neutron flux. Silicon is produced by neutron capture in aluminum, and its presence in structural aluminum can lead to effects on mechanical properties including radiation hardening, loss of ductility, and swelling. The maximum calculated production rates in the cold source aluminum vessel for the HEU and LEU cores at BOC were determined to be 2.8×10^{12} and 3.2×10^{12} $(g\text{-}s)^{-1}$, respectively, and the maximum EOC production rates for both cores were about 3.2×10^{12} $(g\text{-}s)^{-1}$. The BOC volume-averaged production rate for the regions analyzed is about 12.0% greater for the reactor operating with the reference LEU core compared to the reactor operating with the HEU core. The EOC volume-averaged production rate due to the LEU core is about 2.7% greater than that due to the HEU core. The accrual of silicon in the cold source moderator vessel will be slightly greater for the LEU core,

and thus, the aluminum moderator vessel's mechanical property changes due to silicon generation will be slightly greater for the LEU core than for the HEU core.

6. REFERENCES

[1] G. Ilas and R. T. Primm, III, *Low Enriched Uranium Fuel Design with Two-Dimensional Grading for the High Flux Isotope Reactor*, ORNL/TM-2010/318, Oak Ridge National Laboratory, March 2011.

[2] C. O. Slater, R. T. Primm, III, D. A. Pinkston, D. H. Cook, D. L. Selby, P. D. Ferguson, J. A. Bucholz, E. Popov, *Measured and Calculated Heating and Dose Rates for the HFIR HB4 Beam Tube and Cold Source*, ORNL/TM-2009/012, Oak Ridge National Laboratory, March 2009.

[3] C. O. Slater and R. T. Primm, III, *Nuclear Heating Rates in and around the Cold Source and HB4 Beam Tube*, C-HFIR-2005-113, March 2005 (archived, internal document available upon request to the division director, Research Reactors Division, Oak Ridge National Laboratory).

[4] C. O. Slater, *Nuclear Heating Rate in the HFIR Cold Source*, C-HFIR-2005-142, April 2005 (archived, internal document available upon request to the division director, Research Reactors Division, Oak Ridge National Laboratory).

[5] D. Chandler, *Cold Source Nuclear Heating Rates for the HEU and LEU Fueled HFIR*, C-HFIR-2012-014, December 2013 (archived, internal document available upon request to the division director, Research Reactors Division, Oak Ridge National Laboratory).

[6] R. T. Primm, III and N. Xoubi, *Modeling of the High Flux Isotope Reactor Cycle 400*, ORNL/TM-2004/251, Oak Ridge National Laboratory, August 2005.

[7] D. Ilas, *Impact of HFIR LEU Conversion on Spectral Characteristics of Experiment Locations*, ORNL/LTR-2012/414, Oak Ridge National Laboratory, September 2012.

[8] D. Ilas, *Impact of HFIR LEU Conversion on Beryllium Reflector Degradation Factors*, ORNL/TM-2013/441, Oak Ridge National Laboratory, October 2013.

[9] X-5 Monte Carlo Team, *MCNP—A General Monte Carlo N-Particle Transport Code, Version 5*, LA-CP-03-0245, Los Alamos National Laboratory, April 2003.

[10] W. Haeck, *VESTA User's Manual – Version 2.0.0*, Institut de Radioprotection et de Sûreté Nucléaire Report, DSU/SEC/T/2008-331 Indice A, France, 2009.

[11] D. Chandler, R. T. Primm, III, and G. I. Maldonado, *Burnup and Spatially-Dependent Uranium Isotopic Calculations for the High Flux Isotope Reactor*, American Nuclear Society Transaction, Vol. 103, 768 – 769, November 2010.

[12] *SCALE: A Comprehensive Modeling and Simulation Suite for Nuclear Safety Analysis and Design*, ORNL/TM-2005/39, Version 6.1, June 2011 (Available from Radiation Safety Information Computational Center at Oak Ridge National Laboratory as CCC-785), Oak Ridge, TN, 2011.

[13] D. Chandler and R. W. Hobbs, *Neutronics Analyses of NpO_2 Single Pellet Irradiations at HFIR to Support the Pu-238 Production Project*, American Nuclear Society Transaction, Vol . 108, 753-755, June 2013.

[14] MATLAB, Release 2012a, The MathWorks, Inc., Natick, MA.

[15] D. Chandler, *Nuclear Heating and Radionuclide Inventory Calculations to Support NpO2 Single Pellet Irradiations in HFIR*, C-HFIR-2012-006, May 2012 (archived, internal document available upon request to the division director, Research Reactors Division, Oak Ridge National Laboratory).

[16] F. X. Gallmeier and J. C. Gehin, *MCNP-Cross Section Modifications for Reactor Physics Calculations*, Unpublished document, August 1996.

[17] *Chart of Nuclides*, National Nuclear Data Center, Brookhaven National Laboratory, <www.nndc.bnl.gov/chart/>

[18] J. Peterson and G. Ilas, *Calculation of Heating Values for the High Flux Isotope Reactor*, Proceedings of PHYSOR 2012 – Advances in Reactor Physics – Linking Research, Industry, and Education, Knoxville, TN, April 15-20, 2012.

[19] F. B. Brown, W. R. Martin, and R. D. Mosteller, *Monte Carlo – Advances and Challenges*, (workshop presentation at PHYSOR 2008, Interlaken Switzerland), LA-UR-08-05891, Los Alamos National Laboratory, Los Alamos, NM, 2008.

[20] B. R. Betzler, E. E. Sunny, J. C. Lee, and W. R. Martin, *Coupled Nuclear-Thermal-Hydraulic Calculations for Fort St. Vrain Reactor*, NURETH14-421, The 14th International Topical Meeting on Nuclear Reactor Thermalhydraulics, September 2011.

APPENDIX. METHODS AND PREVIOUS CALCULATION COMPARISONS

During the developmental stages of this study, several Monte Carlo N-Particle (MCNP) calculations were executed to compare the different methods and cross section sets being used. The primary purpose of these calculations was to eliminate the need for using specialized cross sections based on the older ENDF/B-V and Institut für Kernenergetik und Energiesysteme (University of Stuttgart, Institute for Nuclear Technology and Energy Systems; IKE) data because it was desired to use the more recent ENDF/B-VII.0 data.

The volume-averaged heat generation rates for the cold source LH_2 and aluminum regions at beginning-of-cycle (BOC) for the high enriched uranium (HEU) core are provided in Table A-1 for several calculations. The results from the calculation labeled as 2005-113 are from [A1], and the results from the calculation labeled as 2005-142 are from [A2]. The ENDF/B-V data and the specialized ^{27}Al, ^{235}U, and LH_2 cross sections (based on ENDF/B-V and IKE) were used in both of these calculations. Calculation 2005-113 used kcode calculations and 2005-142 used fixed source calculations. The surface source was determined by the same input used in 2005-113. Thus, the results from these two calculations should be and are in good agreement with each other (within the statistical uncertainties).

Table A-1. Comparison of average beginning-of-cycle HEU heat generation rates (W/g)

Calculation	k_{eff}	σ_{keff}	LH_2		Aluminum		
			neutron	photon	neutron	photon	beta
2005-113	1.00712	0.00009	4.142	2.746	0.0151	1.526	0.274
2005-142	fixed source		4.200	2.783	0.0154	1.545	0.272
A	1.00717	0.00004	4.144	2.849	0.0150	1.581	0.273
B	1.00996	0.00005	4.188	2.614	0.0146	1.451	0.278
C	1.00996	0.00005	4.172	2.618	0.0147	1.448	0.273
D	1.01274	0.00004	4.020	2.716	0.0145	1.498	0.268
E[a]	0.99716	0.00003	3.935	2.460	0.0142	1.337	0.233

[a] E is the 85 MW HEU BOC calculation documented in the body of this report.

The MCNP input used in [A1] to calculate the source around horizontal beam tube number 4 (HB-4) was used in calculations A, B, C, and D. Therefore, the geometry and material compositions used in the first six calculations listed in Table A-1 are identical except the cold source geometry in 2005-113 is not subdivided into as many cells as the other geometries.

Calculation A was created by replacing the specialized ENDF/B-V ^{235}U cross section library (named 92235.02c) with the default ENDF/B-V ^{235}U cross section library (named 92235.50c) to exclude the delayed photons. The pikmt card was used in a separate run to estimate the delayed photon contribution. As shown in Table A-1, the average neutron energy deposition in the cold source LH_2 decreased by 1.3% and the photon heating increased by 2.3% relative to 2005-142. The only change between the two calculations was the method used in calculating the delayed photon contribution, and therefore, the neutron energy deposition should be equal. The 1.3% decrease in neutron heating falls within the calculated statistical uncertainty (see differences between 2005-113 and 2005-142). A slight increase of 2.3% in the average photon energy deposition shows that the pikmt method is valid and is slightly conservative with respect to using the specialized ^{235}U cross sections (for this application/system).

All three of the specialized cross section libraries (LH_2, ^{235}U, ^{27}Al) were used in calculation B, but the cross sections for all other isotopes were updated to ENDF/B-VII.0 cross sections. This calculation was performed to assess the differences between the two sets of cross sections. The calculated effective multiplication factor increased from 1.00717 to 1.00996 (~36 cents using β_{eff} = 0.00762). These changes caused a decrease of 6.1% (relative to 2005-142) in the average photon heating in the cold source LH_2 regions, a decrease of 5.4% in the average neutron heating in the cold source aluminum, and a decrease of 6.1% in photon heating in the cold source aluminum.

The only difference between calculations C and B is that C used the ENDF/B-VII.0 cross sections for the cold source LH_2, whereas B used the specialized LH_2 cross section library. No differences (within the calculated statistical uncertainties) are observed between the calculations. Thus, it is reasonable to eliminate the use of the specialized LH_2 data and use the ENDF/B-VII.0 data.

Calculation D used the same geometry and material compositions as those used in the calculation to obtain the source around HB-4 for the calculation labeled 2005-142, but the methods and cross sections used in D were the same as those used and described in the set of calculations described in the body of this report. Thus, ENDF/B-VII.0 cross sections were used for all isotopes (including LH_2 and ^{235}U), and the pikmt method was used. The modified ENDF/B-VII.0 ^{27}Al cross section library discussed in the body of this report was also used for calculation D. Relative to 2005-142, the average heating rates decreased between 1.3% and 6.0% for all of the radiation heating means in the cold source LH_2 and aluminum zones.

In conclusion, the largest differences in nuclear heat generation rates between the methods implemented in previous studies [A1–A3] and those used in this calculation are attributable to differences between ENDF/B-V and ENDF/B-VII.0 cross sections. It was shown in this Appendix that the pikmt method produces slightly greater photon heat generation values than those calculated with the specialized ^{235}U data. Also, no statistically identifiable differences were observed in the heat generation rates when using the ENDF/B-VII.0 LH_2 data or the specialized LH_2 data.

As shown in Table A-2, using ENDF/B-VII.0 data and the pikmt method instead of using ENDF/B-V data and specialized cross sections results in average cold source LH_2 and aluminum heating rate differences ranging between 1.3% and 6.0%. Because the cycle 400 model was used in the calculations documented in the body of this report, it is also necessary to examine the effects due to differences between the cycle 400 model and the model used in [A1–A3]. When using the cycle 400 model (labeled E in Tables A-1 and A-2) and the same method as that used in calculation D, the average cold source LH_2 and aluminum heat generation rates range from 6.3% to 14.1% less than those calculated in [A2] (see Table A-2). Since the same cross sections and methods are used for both D and E, the differences between the average cold source LH_2 and aluminum heat generation rates calculated in D and E are attributable to using different models.

The BOC fuel element compositions are the same for both inputs, but the experimental facility loadings differ. The model used in [A1–A3] includes 12 curium targets, a combination of aluminum and stainless steel targets, and aluminum peripheral target positions (PTPs) in the flux trap target region (FTT). The cycle 400 FTT includes mostly shrouded and solid aluminum targets with various PTP loadings (Al, SiC, W, Mo, V, etc.). Although the flux trap loading impacts reactivity, it does not have a large impact on the neutron leakage into the beryllium reflector.

Table A-2. Percent differences between average beginning-of-cycle HEU heating rates

Case	LH_2		Al		
	neutron	photon	neutron	photon	beta
$\frac{[D-(2005\text{-}142)]}{2005\text{-}142}$	−4.29%	−2.39%	−6.04%	−3.04%	−1.25%
$\frac{[E-(2005\text{-}142)]}{2005\text{-}142}$	−6.30%	−11.57%	−7.85%	−13.44%	−14.13%
$\frac{E-D}{D}$	−2.10%	−9.41%	−1.92%	−10.72%	−13.04%

All of the removable beryllium (RB; 8 large and 4 small) and control rod access plug (CRAP; 8) facilities are filled with beryllium plugs in the [A1–A3] model. The cycle 400 model includes beryllium plugs in the CRAP facilities, the small RB facilities, and three of the large RB facilities. However, four of the large RBs are filled with aluminum plugs and one of the RBs has an europium liner and contains experiment materials. The experiment facility loadings near the cold source for the cycle 400 and the [A1–A3] model are shown in Fig. A-1. The loading differences in the RB7A and RB7B facilities between the two models will have the largest impact. The RB7A and RB7B facilities include beryllium plugs in the [A1–A3] model and accommodate europium and aluminum in the cycle 400 model.

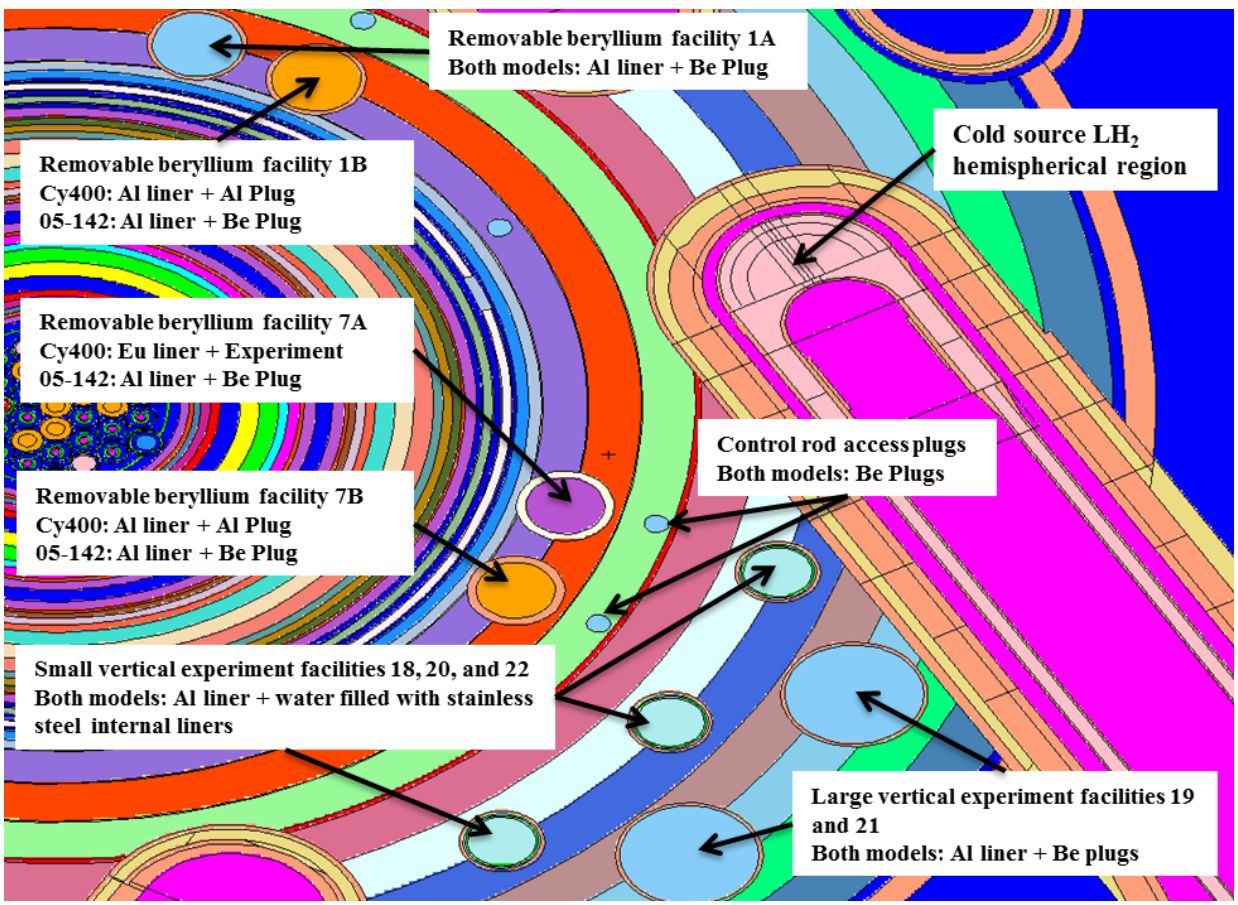

Fig. A-1. Beryllium reflector experiment loading around horizontal beam tube 4.

The isotopic makeup of the control elements (CEs) also differs between the two models. The composition of the CE regions in the [A1–A3] model are fresh (i.e., never irradiated). However, the compositions of the CEs in the cycle 400 model were determined by depletion calculations that account for the irradiation history of the CEs used in cycle 400 [A4 and A5]. The inclusion of "burned" control elements introduces negative reactivity into the core (relative to using fresh CEs) and increases the neutron absorbing capabilities of the elements.

Note that other than the FTT loading, which should have a minimal impact on the cold source heat generation rates, the experiment and CE materials used in the HEU and LEU models are the same.

REFERENCES

[A1] C. O. Slater and R. T. Primm, III, *Nuclear Heating Rates in and around the Cold Source and HB4 Beam Tube*, C-HFIR-2005-113, March 2005 (archived, internal document available upon request to the division director, Research Reactors Division, Oak Ridge National Laboratory).

[A2] C. O. Slater, *Nuclear Heating Rate in the HFIR Cold Source*, C-HFIR-2005-142, April 2005 (archived, internal document available upon request to the division director, Research Reactors Division, Oak Ridge National Laboratory).

[A3] C. O. Slater, R. T. Primm, III, D. A. Pinkston, D. H. Cook, D. L. Selby, P. D. Ferguson, J. A. Bucholz, E. Popov, *Measured and Calculated Heating and Dose Rates for the HFIR HB4 Beam Tube and Cold Source*, ORNL/TM-2009/012, Oak Ridge National Laboratory, March 2009.

[A4] G. Ilas and R. T. Primm, III, *Low Enriched Uranium Fuel Design with Two-Dimensional Grading for the High Flux Isotope Reactor*, ORNL/TM-2010/318, Oak Ridge National Laboratory, March 2011.

[A5] G. Ilas and R. T. Primm, III, *Methodology for Simulating the Irradiation of the Control Elements in HFIR*, American Nuclear Society Transaction, Vol. 103, 396-398, November 2010.

INTERNAL DISTRIBUTION

1. B. J. Ade (*adebj@ornl.gov*)
2. K. J. Beierschmitt (*beierschmitt@ornl.gov*)
3. G. I. Bell (*bellgi@ornl.gov*)
4. S. M. Bowman (*bowmansm2ornl.gov*)
5. D. Chandler (*chandlerd@ornl.gov*)
6. D. H. Cook (*dhc@ornl.gov*)
7. R. A. Crone (*cronera@ornl.gov*)
8. R. J. Ellis (*ellisrj@ornl.gov*)
9. J. D. Freels (*freelsjd@ornl.gov*)
10. J. C. Gehin (*gehinjc@ornl.gov*)
11. C. R. Hyman (*hymancriii@ornl.gov*)
12. A. S. Icenhour (*icenhouras@ornl.gov*)
13. G. Ilas (*ilasg@ornl.gov*)
14. P. K. Jain (*jainpk@ornl.gov*)
15. M. W. Kohring (*kohringmw@ornl.gov*)
16. Y. S. Kwon (*kwonys@ornl.gov*)
17. R. S. McKeehan (*mckeehanrs@ornl.gov*)
18. C. V. Parks (*parkscv@ornl.gov)*
19. J. L. Peterson (*petersonjl@ornl.gov*)
20. D. L. Pinkston (*pinkstondl@ornl.gov*)
21. T. Powers (*powerstp@ornl.gov*)
22. D. G. Renfro (*renfrodg@ornl.gov*)
23. K. A. Smith (*smithka@ornl.gov*)
24. E. E. Sunny (*sunnyee@ornl.gov*)
25. W. J. Toth (*tothwj@ornl.gov*)
26. ORNL Laboratory Records (*hamrindr@ornl.gov*)
27. RRD-DCC-RC (*hugginscn@ornl.gov*)

EXTERNAL DISTRIBUTION

28. A. Adams, U.S. Nuclear Regulatory Commission, One White Flint North, 11555 Rockville Pike, Rockville, Maryland 20852-2738 (*axa@nrc.gov*)
29. Aurelien Bergeron, Argonne National Laboratory, 9700 S. Cass Avenue, Argonne, IL 60439 (*abergeron@anl.gov*)
30. Douglas Burkes, Pacific Northwest National Laboratory *(douglas.burkes@nnsa.doe.gov)*
31. R. A. Butler, Director, Research Reactor Center, 1513 Research Park Drive, Columbia, MO 65211 (*ButlerRa@missouri.edu*)
32. G. S. Chang, Idaho National Laboratory, P.O. Box 1625, Idaho Falls, ID 83415-3885 (*gray.chang@inl.gov*)
33. M. D. DeHart, Idaho National Laboratory, P.O. Box 1625, Idaho Falls, Idaho 83415-8370 (*Mark.DeHart@inl.gov*)
34. D. Diamond, Brookhaven National Laboratory, P.O. Box 5000, Upton, NY 11973-5000 (*diamond@bnl.gov*)
35. J. Dwight, Idaho National Laboratory, P.O. Box 1625, Idaho Falls, ID 83415-3750 (*John.Dwight@inl.gov*)
36. L. Foyto, Research Reactor Center, 1513 Research Park Drive, Columbia, MO 65211 (*foytol@missouri.edu*)
37. D. Kutikkad, Assistant Reactor Manager-Physics, University of Missouri Research Reactor Facility, Columbia, MO 65211 (*kutikkadk@missouri.edu*)
38. C. Landers, NA-212, U.S. Department of Energy, 1000 Independence Avenue SW, Washington, DC 20585 (*Christopher.landers@nnsa.doe.gov*)
39. J. Matos, Argonne National Laboratory, 9700 S. Cass Avenue, Argonne, IL 60439 (*jim.matos@anl.gov*)
40. D. McDaniel, Idaho National Laboratory, P.O. Box 6188, Idaho Falls, ID 83415 (*David.McDaniel@inl.gov*)
41. C. McKibben, University of Missouri Research Reactor Facility, Columbia, MO 65211 (*mckibbenj@missouri.edu*)
42. Mitch Meyer, P.O. Box 1625, Idaho Falls, ID 83415-3750 (*Mitchell.Meyer@inl.gov*)
43. J. O. Moore, U.S. Department of Energy (*moorejo@ornl.gov*)
44. S. R. Morrell, Idaho National Laboratory (*sean.morrell@inl.gov*)
45. T. Newton, MIT Nuclear Reactor Laboratory, 138 Albany St., Cambridge, MA 02139 (*tnewton@mit.edu*)
46. S. O'Kelly, NIST Center for Neutron Research, 100 Bureau Drive, Stop 8560, Gaithersburg, MD 20899-8560 (*sean.okelly@nist.gov*)
47. R. T. Primm III, Primm Consulting, Laurel Hill Road, Knoxville, TN 37923 (*trentprimm@primmconsultingllc.com*)
48. D. Reed, U.S. Department of Energy (*reeddr@ornl.gov*)

49. W. Richards, NIST Center for Neutron Research, 100 Bureau Drive, Stop 8561, Gaithersburg, MD 20899-8561 (*wade.richards@nist.gov*)
50. J. Roglans, Argonne National Laboratory, 9700 S. Cass Avenue, Argonne, IL 60439 (*roglans@anl.gov*)
51. K. E. Rosenberg, Idaho National Laboratory (*kenneth.rosenberg@inl.gov*)
52. D. Rosine, U.S. Department of Energy (*rosinedb@ornl.gov*)
53. C. Sohn, Office of Basic Energy Sciences, U.S. Department of Energy, 1000 Independence Avenue SW, Washington, DC 20585 (*carol.sohn@pnso.science.doe.gov*)
54. P. Staples, NA-212, U.S. Department of Energy, 1000 Independence Avenue SW, Washington, DC 20585 (*Parrish.Staples@nnsa.doe.gov*)
55. J. G. Stevens, Argonne National Laboratory, 9700 S. Cass Avenue, Argonne, IL 60439 (*johnstevens@anl.gov*)
56. D. M. Wachs, MFC 791 B-147, Idaho National Laboratory, P.O. Box 6188, Idaho Falls, ID 83415 (*Daniel.Wachs@inl.gov*)
57. R. E. Williams, NIST Center for Neutron Research, 100 Bureau Drive, Stop 8560, Gaithersburg, MD 20899-8560 (*robert.williams@nist.gov*)
58. E. H. Wilson, Argonne National Laboratory, 9700 S. Cass Avenue, Argonne, IL 60439 (*erikwilson@anl.gov*)
59. E. C. Woolstenhulme, P.O. Box 1625, Idaho Falls, ID 83415-3750 (*Eric.Woolstenhulme@inl.gov*)